Thermodynamic and Kinetic Properties of Materials for Next-Generation Rechargeable Batteries from First-Principles

by

Alexandra Emly

A dissertation submitted in partial fulfillment
of the requirements for the degree of
Doctor of Philosophy
(Materials Science and Engineering)
in The University of Michigan
2015

Doctoral Committee:

Associate Professor Anton Van der Ven, Co-Chair
Assistant Professor Emmanouil Kioupakis, Co-Chair
Assistant Professor Pierre Ferdinand Poudeu-Poudeu
Assistant Professor Donald J. Siegel

ACKNOWLEDGEMENTS

First and foremost, I would like to graciously thank my wonderful advisor, Anton Van der Ven, without whom I never would have even started research in this area and who always gave wonderful answers to the many questions I have had throughout these four years. I could not imagine a better advisor. Secondly, to Manos, thank you for "adopting" me when Anton moved to Santa Barbara - I appreciate the support immensely. Thank you to my committee members, Ferdinand Poudeu and Don Siegel, as well as members of the Van der Ven and Kioupakis groups, in particular Anna Belak, Ivy Chen, Donghee Chang, and Dylan Bayerl. To conclude the "academic" thanks, thank you to Shirley Meng who introduced me to the world of research my sophomore year at University of Florida. I am sure my path would have been vastly different had I not joined your lab back in 2008.

I thank my parents and family for blindly supporting me throughout my eight years delving into the world of materials science. Words can not do justice to the unwavering support and guidance you have all provided me, and I thank you for enabling me to become the person I am. Piggy-backing off of growing up, thank you to all the teachers over the last two decades who have inspired and enabled me to pursue science and engineering.

Most of all, I thank my soon-to-be husband, Daniel Ortiz, whose patience, love, and perseverance while undertaking his own PhD was absolutely vital in this success. I look forward to our post-PhD life immensely.

TABLE OF CONTENTS

ACKNOWLEDGEMENTS ii

LIST OF FIGURES v

ABSTRACT x

CHAPTER

I. Introduction 1

1.1 Current Li-Ion Battery Technology & Shortcomings 1
1.1.1 Electrode Materials 2
1.1.2 Electrolyte Materials 3
1.2 Current Research in Next-Generation Rechargeable Battery Systems 4
1.2.1 Solid Electrolytes 4
1.2.2 Mg-ion Batteries 5
1.2.3 Na-ion Batteries 6
1.3 Motivation & Topic Organization 6
1.3.1 Solid Electrolytes 7
1.3.2 Magnesium Batteries 7
1.3.3 Sodium Batteries 8

II. Theoretical Background & Computational Methods 10

2.1 Thermodynamics & Statistical Mechanics Principles 10
2.2 Cluster Expansion Formalism 12
2.3 First Principles Calculations 14
2.3.1 Local Density and Generalized Gradient Approximations 17
2.3.2 van der Waals Corrections to the Generalized Gradient Approximation 17
2.3.3 Hybrid Functional Calculations 19

2.3.4 Shortcomings 20

III. Solid Electrolyte Li_3OX (X=Cl,Br) 22

3.1 Introduction 23
3.2 Phase Stability 24
3.2.1 Phase Stability in the Li-Cl-O & Li-Br-O Composition Space 25
3.2.2 Electronic Structure 30
3.2.3 Phase Stability as a Function of Lithium Chemical Potential (μ) 31
3.3 Conductivity 34
3.3.1 Charge Carriers: Finding Defects 35
3.3.2 Diffusion Pathways 41
3.4 Conclusions 45

IV. Mg_xTiS_2 as a Cathode for Mg-ion Rechargeable Batteries 46

4.1 Phase Stability 47
4.1.1 Global Phase Stability 47
4.1.2 Phase Stability in the O1 Phase 49
4.1.3 Phase Stability in the Spinel Phase 51
4.1.4 Voltage Predictions 51
4.2 Diffusion 53
4.2.1 Diffusion in Layered O1 Structure 53
4.2.2 Diffusion in Spinel Structure 58
4.3 Charge Distribution 59
4.4 Discussion 64
4.5 Conclusions 66

V. Na_xCoO_2 as a Cathode for Na-ion Rechargeable Batteries 68

5.1 Phase Stability 68
5.2 Diffusion Mechanisms 70

VI. Conclusions & Outlook 71

BIBLIOGRAPHY 72

LIST OF FIGURES

Figure

1.1 Schematic of a Li-ion battery: the cathode (positive electrode) and anode (negative electrode) sandwich the electrolyte, a typically-liquid medium through which only Li ions migrate. 2

1.2 Two-dimensional layered intercalation crystal structures: O1 (a), O3 (b), spinel (c), P2 (d), P3 (e). Transition metals sit at the centers of the purple octahedra and are coordinated by six sulfur/oxygen atoms shown as small yellow spheres. Lithium intercalates into the empty layers into sites shown by green spheres. 3

1.3 β-alumina, a sodium-ion conductor. Na ions partially fill the yellow sites and β-alumina serves as the backbone structure with O (red) coordinating the Al atoms (at centers of octahedra and tetrahedra). 5

2.1 Clusters on a two-dimensional triangular lattice. Lithium atoms/vacancies randomly decorate the structure as red/blue circles 13

2.2 Calculated c- and a-lattice parameters for Mg_xTiS_2 (0¡x¡0.5) using different approximations to DFT. Solid lines correspond to PBE with vdW-DF corrections to account for the vdW forces. Dashed lines correspond to LDA (black) and standard PBE (yellow), while the purple dot-dashed line corresponds to HSE06 18

3.1 Li_3OCl with the antiperovskite crystal structure. Li occupy the face-centered sites, O occupies the body-centered site, and Cl occupy corner sites. 24

3.2 a) Defect-free Li_3OCl (reprinted to show differences between this structure and (b) and (c). b) Stable Li_5O_2Cl structure. The oxygen octahedra distort to allow for corner sharing of lithium atoms because of the two LiCl vacancies present in this supercell. c) Stable $Li_{17}O_6Cl_5$ structure. The structure distorts slightly to compensate for the LiCl vacancy. 26

3.3 Calculated LiCl-Li-Li_2O_2 and LiBr-Li-Li_2O_2 phase diagrams. a) Stable LiCl-Li-Li_2O_2 phase diagram. b) metastable LiCl-Li-Li_2O_2 phase diagram assuming kinetic suppression of Li_2O formation. Three new phases become stable: α, Li_3OCl; β $Li_17O_6Cl_5$; γ Li_5O_2Cl. c) Stable LiBr-Li-Li_2O_2 phase diagram. d) Meta-stable LiBr-Li-Li_2O_2 phase diagram assuming kinetic suppression of Li_2O. Li_3OBr and Li_5O_2Br (γ) are stable. 28

3.4 Different polymorphs of Li_3OCl with unit cells shown in black boxes. a) phonon band structure of cubic $Fm\bar{3}m$ Li_3OCl. b) 2x2x3 supercell of cubic Li_3OCl. c) low-energy polymorph structure $Pna2_1$ with octahedral tilts in all three directions. d) lowest-energy polymorph structure P2/m with octahedral tilts in two directions. 30

3.5 Electronic Band Diagram of a) Li_3OCl and b) Li_3OBr calculating using HSE06 hybrid pseudopotential 31

3.6 Oxygen/Chlorine composition versus Li chemical potential phase diagram calculated assuming suppression of Li_3OCl decomposition into LiCl and Li_2O. Metastable Li_3OCl can resist decomposition up to an applied voltage (relative to metallic Li) of 2.55V whereas the two other stable Li_2O-rich phases will decompose at lower voltages around 2.1V. LiO_4Cl appears above 2.92V. 33

3.7 Energetically stable Li dumbbell interstitial (split interstitial). An interstitial prefers to split a Li site of an Li_6O octahedron effectively sharing the site (two blue atoms). It resides in the face shared with the four chlorine corner atoms. The dumbbell has two symmetrically equivalent stable orientations parallel to the axes of the anti-perovskite cubic unit cell 36

3.8 Mixing energies of off-stoichiometric antiperovskite derived phases. (a) shows various ways of deviating from the ideal anti-perovskite Li_3OCl stoichiometry from the range Li_2O (x=0) to LiCl (x=1). (b) is an enlarged portion of the gray box in (a). Substitutions on the O/Cl sub lattices, interstitials, and vacancies are denoted by diamonds, circles, and squares, respectively. Li_2O-rich structures have compositions x < 0.50 and LiCl-rich structures have compositions with x>0.50. Substitutions on the halogen sublattice have the lowest mixing energies. The defect-free antiperovskite is shown as a black star. 38

3.9 Lithium migration around the edge of a Li_6O octahedron into a vacant site (black with dotted white line). The barrier ranges from 310 meV to 380 meV for neutral and charged vacancies in Li_3OCl and Li_3OBr 41

3.10 Low-barrier migration pathway for a neutral Li split interstitial in Li_3OCl. The barriers range from 145 meV to 175 meV depending on the charge state of the interstitial (neutral or +1) and host material (Li_3OCl or Li_3OBr 42

3.11 Alternative migration pathways for a dumbbell interstitial. (a) shows a perpendicular rotation to switch planes of movement, while (b) shows an in-plane rotation. 43

3.12 Migration barriers for local $Li_3OCl_{0.5}Br_{0.5}$ environments. Br is denoted by yellow spheres with red pluses while Cl are denoted by green spheres. 44

4.1 Formation energies calculated with PBE and the optB86 vdW correction for the spinel and various layered forms of Mg_xTiS_2. The O1 structure is the most stable across the entire composition range. Colors and shapes indicate different stacking sequences 48

4.2 Formation energies from composition TiS_2 (x=0) to $Mg_{0.5}TiS_2$ (x=0.5) for all stacking sequences with LDA (a), opt-B86 (b), and opt-B88 (c). Qualitative trends remain the same across all three calculation schemes. 49

4.3 Mg in-plane ordering in the three most stable ground states of O1 Mg_xTiS_2 ($0 \leq x \leq 0.5$) along with projections of the Mg ordering within the intercalation layers. Yellow triangles denote potential octahedral Mg sites. Red circles correspond to Mg ions in one layer while yellow circles denote Mg atoms occupying the adjacent layer. Sulfur atoms occupy the vertices of each triangle. The white triangles denote tetrahedral sites 50

4.4 Calculated 0K hulls in the O1 phase using LDA (left), optB88 (middle), and optB86 (right). All three show the same ground state ordering. The green line with squares are the predicted cluster-expanded ground states, and the blue line with circles are the DFT ground states 50

4.5 The O1 Mg_xTiS_2 voltage curve calculated with Monte Carlo simulations at 300K applied to a cluster expansion that was parameterized with PBE-optB86 (red), opt-B88 (blue), and LDA (green) energies. 52

4.6 The spinel Mg_xTiS_2 voltage curve calculated with Monte Carlo simulations at 300K applied to a cluster expansion that was parameterized with PBE-optB86 (red), opt-B88 (blue), and LDA (green) energies . 53

4.7 Migration pathway and barrier in dilute, O1 $MgTi_{32}S_{64}$. The pathway shows the motion of a Mg atom from an octahedral site (α) into an adjacent octahedral site (δ) through tetrahedral site which is a local minimum (γ). The maximum energy occurs when Mg passes through the trigonal face (β) shared by the octahedral and tetrahedral site. 54

4.8 Energy differences between octahedral and tetrahedral sites in dilute O1 $MgTi_{32}S_{64}$. The dashed red line denotes the experimental c lattice parameter for TiS2 (5.7[77],[83]) and bond lengths are shown for the PBE-optB86 relaxed lattice parameters of TiS_2 and for a 10% increase of the c lattice parameter. Percentage increases are shown in italicized parentheses for the 10% expansion figure. 54

4.9 Effect of c lattice parameter increases on the migration barrier in dilute O1 $Mg_{1/32}TiS_2$. Energy barriers are shown in (a) for the equilibrium PBE+optB86 TiS_2 lattice parameters (black, top) and for a c-lattice parameter that is expanded by 5% (blue, middle) and 10% (green, bottom). Schematics of bond length increases are shown with the same color scheme in b 56

4.10 Mg hop in layered O1 $Mg_{1/3}TiS_2$. (a) Migration pathway from an octahedral site (α) to a local minimum at a tetrahedral site (purple, β) into an adjacent edge-sharing octahedron (γ, green). (b) Diffusion energy barrier and (c) Hop path as projected along the c-axis into the plane of the intercalation layer 56

4.11 Mg hop in layered O1 $Mg_{1/2}TiS_2$. (a) Migration pathway from an octahedral site (α) to a local minimum at a tetrahedral site (purple, β) into an adjacent edge-sharing octahedron (γ, green). (b) Diffusion energy barrier and (c) Hop path as projected along the c-axis into the plane of the intercalation layer 57

4.12 Diffusion in dilute $MgTi_{32}S_{64}$ in the spinel structure. (a) shows the diffusion barrier across path shown in (b). The black line with squares shows the barrier at equilibrium $Ti_{32}S_{64}$ lattice parameters calculated with GGA and optB86 for the van der Waal's correction. The blue line with circles shows the barrier if the volume is expanded 5%. . . 58

4.13 The effect of a volume increase on the difference in energy between tetrahedral versus octahedral occupancy by Mg in spinel $MgTi_{32}S_{64}$. The dashed red line shows the experimental lattice parameter at 9.737A[84] of spinel TiS_2. Bond lengths are shown for the relaxed structures for the PBE-optB86 TiS_2 parameters and for lattice parameters corresponding to a 10% increase in volume. 59

4.14 Charge difference plots of layered TiS_2 having the O1 crystal structure with an isolated Mg (x=$\frac{1}{32}$ in (a) an octahedral site and (b) a tetrahedral site and with an isolated Li (x=$\frac{1}{32}$) (c) in an octahedral site and (b) in a tetrahedral site. Blue regions denote areas of charge depletion while yellow regions denote charge accumulation. The intercalating species sits at the center of the yellow cloud of charge accumulation and is coordinated by sulfur atoms (black) and further out sit Ti atoms (purple). Ti-S bonds are drawn to better show d orbital rehybridization 61

4.15 Charge difference plots of layered TiS_2 in either the O1 or spinel crystal structure with an isolated Mg (x=$\frac{1}{32}$ in a tetrahedral site. Blue regions denote areas of charge depletion while yellow regions denote charge accumulation. All S-S bonds are identical for both spinel and O1 to isolate effects the Ti environment has on charge rehybridization. All atoms not undergoing charge re-hybridization have been hidden for clarity. The spinel structure has 12 Ti atoms participating in charge re-hybridization located in four groups of three Ti atoms, while the O1 structure has 9 Ti atoms participating in charge rehybridization, with one group of three shown at the top of (a) and the remaining six clustered in a network at the bottom of (a). 63

5.1 Formation energies for calculated structures along composition Na_xCoO_2 with $0 \leq x \leq 1$. Blue triangles denote structures where the sodium ions all relaxed into tetrahedral sites, open red diamonds denote structures where the sodium ions all relaxed into octahedral sites, and green stars show structures where sodium ions fill both octahedral and tetrahedral sites. 69

5.2 Diffusion pathway for dilute $NaCo_{32}O_{64}$ from a tetrahedral site (α) to another tetrahedral site through an octahedral site (β) 70

ABSTRACT

Thermodynamic and Kinetic Properties of Materials for Next-Generation Rechargeable Batteries from First-Principles

by

Alexandra Emly

Chairs: Anton Van der Ven and Emmanouil Kioupakis

To break out of small electronics and into vehicles, rechargeable battery technology needs to overcome several obstacles. First, safety issues plague the usage of liquid electrolytes in traditional Li-ion battery systems. Secondly, alternative elements to Li would be more earth-abundant as well as potentially have higher capacities. With these factors in mind, we will discuss thermodynamic and kinetic properties from first-principles calculations surrounding three next-generation materials for rechargeable batteries: a solid electrolyte, Li_3OCl, for use in Li-ion batteries. a magnesium battery electrode (Mg_xTiS_2), and a sodium battery electrode (Na_xCoO2).

First, we explore diffusion in Li_3OX (X=Cl, Br), a superionic conductor with experimental conductivities on the order of 1 $mScm^{-1}$. These compounds, which have an anti-perovskite crystal structure, have potential applications as solid electrolytes in Li-ion batteries to replace the currently-employed liquid electrolytes. We identify a low-barrier three-atom hop mechanism involving Li interstitial dumbbells. This hop mechanism is facile within the (001) crystallographic planes of the perovskite crystal

structure and is evidence for the occurrence of concerted motion, similar to ionic transport in other solid electrolytes. Our first-principles analysis of phase stability predicts that antiperovskite Li_3OCl (Li_3OBr) is metastable relative to Li_2O and LiCl (LiBr) at room temperature.

Second, we examine the thermodynamic and kinetic properties of Mg_xTiS_2 and compare it to its well-known analog, Li_xTiS_2 in order to better understand the difficulties obtaining facile diffusion in Mg-ion batteries. We show that although thermodynamically, the two systems are incredibly similar, the extra electron that Mg has over Li hinders diffusion immensely.

Thirdly, we briefly investigate the spinel Na_xCoO_2. Unlike any other spinel structure where intercalating species first occupy all tetrahedral sites then proceed to occupy octahedral sites, with sodium, both octahedral and tetrahedral sites are filled at various compositions leading to some unique thermodynamic and kinetic results.

CHAPTER I

Introduction

First commercialized by Sony in 1991, lithium-ion batteries (LIBs) continue to power small devices today. Given today's necessity for cleaner energy, batteries are being heralded to store energy from more renewable sources (e.g. solar and wind) as well as to replace traditional fuel in vehicles. However, if LIBs (and rechargeable batteries in general) are to be successfully implemented in new technology and move beyond the small devices they have been powering, improvements must be made to the materials used in fabricating battery elements. We explore different materials systems using first principles calculations to help elucidate issues plaguing successful implementation.

1.1 Current Li-Ion Battery Technology & Shortcomings

A battery (as shown in Figure 1.1) is comprised of two solid electrodes and an electrolyte (typically a liquid); lithium ions flow between the positive cathode and the negative anode through the electrolyte while the electron moves through an external circuit. During discharge, ions move from the anode into the cathode, and during charge, lithium ions move from the cathode back into the anode. The voltage of a battery is proportional to the difference in the chemical potential of lithium (μ_{Li}) between the anode and the cathode; by definition, the cathode has a higher voltage

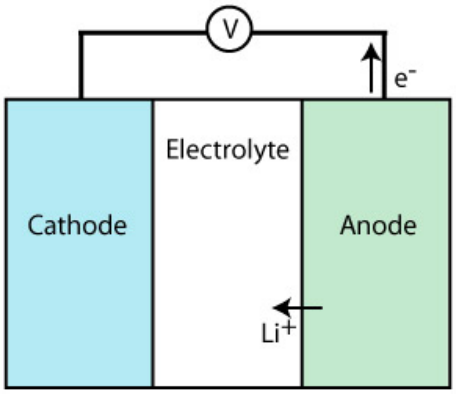

Figure 1.1: Schematic of a Li-ion battery: the cathode (positive electrode) and anode (negative electrode) sandwich the electrolyte, a typically-liquid medium through which only Li ions migrate.

with respect to a reference electrode than the anode. The capacity, or the amount of energy able to be stored, of the battery is an inherent material property related to the number of lithium that can intercalate into the two electrodes. Different factors including poor kinetics and structural changes upon lithiation prevent materials from reaching their theoretical capacity.

For the last few decades, commercial Li-ion batteries have been comprised of a graphite anode, liquid electrolyte containing polymer solvents and a lithium salt and $LiCoO_2$. Graphite has two-dimensional sheets weakly held together by van der Waals forces, and lithium can easily intercalate to form LiC_6; the cathode usually is a transition metal intercalation material, similarly layered with channels for lithium migration. As the battery is charged, lithium ions move from the cathode into the anode, and vice versa for discharging.

1.1.1 Electrode Materials

Common cathodes are typically characterized as intercalation materials, where the host structure is usually a transition metal chalcogenide (e.g. Mn_2O_4, TiS_2) and lithium ions shuttle in the crystal structure's layers. These structures can accommodate lithium across a wide composition range with minimal structural change to the

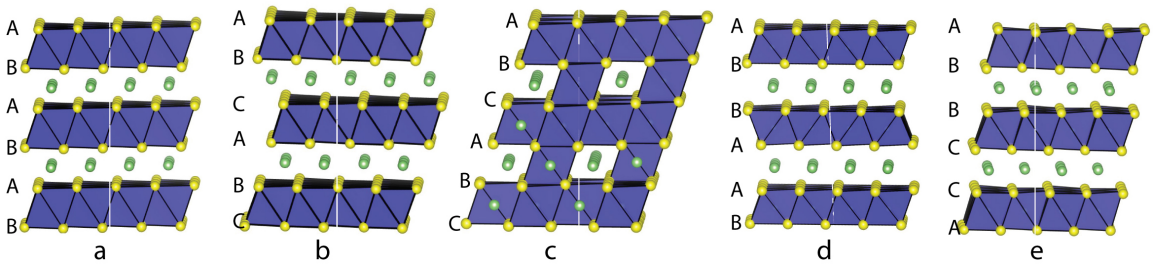

Figure 1.2: Two-dimensional layered intercalation crystal structures: O1 (a), O3 (b), spinel (c), P2 (d), P3 (e). Transition metals sit at the centers of the purple octahedra and are coordinated by six sulfur/oxygen atoms shown as small yellow spheres. Lithium intercalates into the empty layers into sites shown by green spheres.

host. This makes them ideal for use in batteries because structural changes (such as phase transformations and large expansions upon the addition of lithium) can cause a battery to fail. Diffusion occurs through one- (e.g. $LiFePO_4$), two- (e.g. $LiTiS_2$, $LiCoO_2$) or three-dimensional (spinel structures) channels. The spinel structure has the same stacking of close-packed oxygen (or sulfur) planes as the ABC layered structure (O3), however, mixing occurs throughout the transition metal and lithium layers - $\frac{1}{4}$ of the intercalating species sits in the transition metal layer while $\frac{1}{4}$ of the transition metal resides in intercalating species layer.

Different common stacking sequences for two-dimensional intercalation materials are shown in Figure 1.2. Stacking sequences are characterized by the stacking of the close-packed oxygen (or sulfur) planes, and the intercalating species (e.g. Li) and transition metal (e.g. Ti, Mn, Co) alternate filling the close-packed planes. Small ions like Li tend to stack in O1, O3, or spinel (Figures 1.2a-c), whereas larger ions like Na tend to prefer the trigonal prismatic structures, shown in Figures 1.2d,e.

1.1.2 Electrolyte Materials

Electrolyte materials in use today are most often liquids comprised of polymer solvents and a lithium salt, such as $LiPF_6$. However, since these liquids operate

at voltages outside their stability window, these electrolytes suffer from a variety of drawbacks[1] including the off-gassing of polymer solvents (such as O_2 and CO_2 gas), decomposition leading to the formation of what is commonly called the solid electrolyte interphase (SEI) layer, and safety concerns preventing the usage of metallic lithium in batteries. In theory, solids should eliminate many of these issues, however, conductivity has not reached adequate levels for usage in batteries until recently. Solid electrolytes should in principle overcome many of these problems.

For implementation in battery systems, three key things must be considered for solid electrolytes: electrochemical stability, conductivity, and phase stability. The electronic band gap can serve as an upper limit for the electrochemical stability [2], and calculating the grand canonical free energy at varying chemical potentials can show voltages at which structures will break down. Conductivity is the product of the number of carriers combined with the ease of diffusion. Phase stability is also key to maintain structural integrity of the compound as ions diffuse through it.

1.2 Current Research in Next-Generation Rechargeable Battery Systems

1.2.1 Solid Electrolytes

The most well-known solid electrolyte is β -alumina (shown in Figure 1.3, which is a sodium-ion conductor where sodium ions migrate through channels of Al_2O_3 sheets. Although many of the safety issues plaguing liquid electrolytes are eliminated by moving to a solid material, conductivity usually is much lower in solid electrolytes than in their liquid counterparts, especially in early solid electrolytes Li_3N[3] and LIPON[4], which at room temperature have conductivities several orders of magnitude lower than those of their liquid counterparts.

The past decade[5],[6] has seen the discovery of new solid electrolytes with sig-

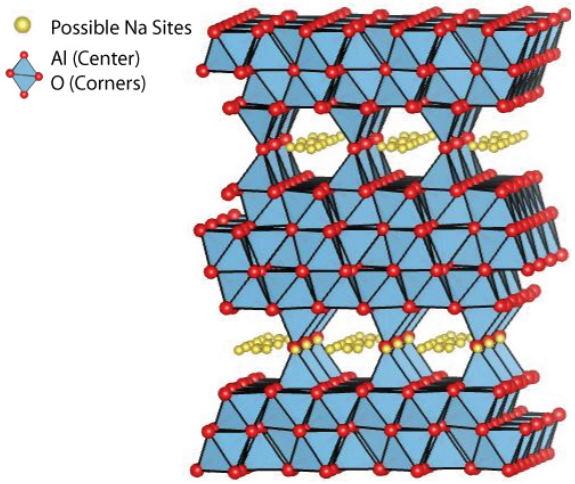

Figure 1.3: β-alumina, a sodium-ion conductor. Na ions partially fill the yellow sites and β-alumina serves as the backbone structure with O (red) coordinating the Al atoms (at centers of octahedra and tetrahedra).

nificantly in-creased ionic conductivities, making them potentially feasible for use in lithium-ion batteries. The discovery of $Li_{10}GeP_2S_{12}$[7] (LGPS), with a conductivity of 12 $mScm^{-1}$, opened the door to the possibility that solid electrolytes could outperform liquid electrolytes. Research has increased tremendously on both the theoretical[8],[9],[10],[11] and experimental[5],[6],[12],[13] side of solid electrolytes.

LGPS as well as other known solid electrolytes usually consist of wide, open structures which have a high number of vacant sites relative to filled sites to allow for easy ionic diffusion. The host structure of LGPS consists of channels created from a LiS_6 backbone through which Li atoms can easily diffuse.

1.2.2 Mg-ion Batteries

Although research on magnesium batteries began around the same time as it did on lithium batteries, progress has been much slower for Mg rechargeable batteries. Mg-ion batteries could be a promising alternative to Li-ion batteries because of the natural abundance of Mg, its lower cost and the possibility of achieving increased capacity and energy density. Additionally, the ionic radii of Li and Mg are quite

similar, implying that host structures could share similarities. One advantage of a Mg battery is the possible use of pure Mg as the anode as it is less susceptible to dendrite formation compared to Li metal anodes[14],[15]. However, while the properties associated with the intercalation of both Mg- and Li-ions into a variety of compounds were investigated in the 1990s[16],[17],[18], only Li-ion battery technology has progressed significantly.

Decades of fundamental research on Li-ion batteries has shown that a surprisingly large number of materials classes can react electrochemically with Li, offering a wide variety of chemistries to select from for the electrodes of Li-ion batteries. This broad spectrum of candidate Li-electrode materials suggests that unexplored chemistries may also exist that can react with Mg electrochemically and that simultaneously overcome the low mobilities that typify Mg in crystalline solids. This possibility has spurred a renewed interest in Mg-ion batteries[19],[20].

1.2.3 Na-ion Batteries

In light of the concerns of increasing costs and decreasing abundance of lithium, sodium has re-emerged as a more environmentally- and cost-friendly battery system. When gravimetric energy density is not a vital factor, sodium-ion batteries can provide a superior alternative to lithium-ion batteries. Sodium ions are larger than lithium ions and thus show a tendency to favor different crystallographic sites (e.g. trigonal prismatic) than those often occupied by lithium (e.g. octahedral and tetrahedral).

1.3 Motivation & Topic Organization

First-principles calculations can help to understand many issues plaguing lithium-ion batteries through examining problems at an atomic scale and isolating specific effects. This can help experimentalists better understand systems already under in-

vestigation while also guiding investigators to study systems with similar properties. For this reason, we focus on material systems beyond traditional Li-ion rechargeable systems. With electrode systems, we can study the stable phases across an entire composition range that would exist during charging or discharging. With solid electrolytes, we can examine precisely how migration of Li atoms is occurring throughout the material. We further explain methodology in Chapter II. Conclusions and an outlook for the future of rechargeable battery systems are presented in Chapter VI. The following topics are highlighted in this thesis for the below reasons.

1.3.1 Solid Electrolytes

In light of the many shortcomings of liquid electrolytes discussed previously, we focus on solid electrolytes. As mentioned, many solid electrolytes achieve high conductivity through structures with a large number of vacant sites intrinsically in the structure. However, in 2012 a material (Li_3OCl) was found to achieve comparable conductivities[12] to that of its vacancy-rich solid electrolytes even though Li_3OCl has no intrinsic vacant sites in its antiperovskite structure. For this reason, we chose to explore diffusion and phase stability within this structure to explain the high conductivity achieved experimentally. In Chapter III, we explain the reason for high conductivity achieved experimentally for a system which differs substantially from other known solid electrolytes. We also point to ways to increase the conductivity further through introducing defects at the synthesis stage and report on which defects are most likely to form.

1.3.2 Magnesium Batteries

There is currently a lack of fundamental insight as to the differences between Li-intercalation compounds and their Mg analogs. Although several experimental studies[21],[18],[22],[23],[24] have compared Mg-based electrodes to their Li counter-

parts, few computational studies have been reported on[25],[26]. The only structures found to have moderate Mg diffusion to date are Chevrel phases[27][28]. While the atomistic mechanism of Mg diffusion in the Chevrel phases remain poorly understood, the presence of a cluster of transition metal atoms surrounding the Mg sites seems crucial to accommodate the more positive valence of Mg and facilitate high Mg mobilities. The Chevrel crystal structures, however, have little in common with typical Li-ion intercalation compounds. To date, no fundamental studies of the electrochemical properties of Mg in important Li-intercalation host chemistries and crystal structures have been reported. It is not clear, for example, whether Mg will intercalate within the layered or spinel host structures widely used in Li-ion batteries, and if they do, with which rates. Even though it is assumed that the extra electron Mg carries is a key factor in poor kinetics, a substantial investigation into the kinetic difficulties has not yet been studied. We thoroughly examine kinetic and thermodynamic properties of the Mg_xTiS_2 system in Chapter IV; its Li counterpart is well-known, and provides a good system to isolate thermodynamic and kinetic effects between systems with one electron (Li) and two electrons (Mg) in the intercalating species. Although the Mg_xTiS_2 system is thermodynamically very similar to the Li_xTiS_2 system, the kinetic properties vary substantially. This leads us to conclude that for successful Mg battery implementation, research needs to focus on systems that are structurally very different (e.g. Chevrel phases[27]) from current Li-ion battery systems (e.g. olivine, layered, spinel structures).

1.3.3 Sodium Batteries

Finally, we explore a sodium battery system (spinel Na_xCoO_2) in Chapter V. Although Na and Li both have one electron, the larger ionic radius of sodium alters the thermodynamic stability of different phases. Although in dilute composition ranges, sodium actually has a lower diffusion barrier than lithium, at larger compositions, the

diffusion of sodium is hindered. Interestingly, this is in complete contrast to the Mg system which thermodynamically is very similar to its Li analog while the kinetics of diffusion differs drastically.

CHAPTER II

Theoretical Background & Computational Methods

Computational modeling has been utilized not just to confirm experimental findings, but on countless occasions, it has also helped elucidate complex issues that are inaccessible to measurement techniques thereby helping to explain and further the understanding of engineering problems. At the smallest length scale, atomic interactions dictate macroscopic properties of solids.

2.1 Thermodynamics & Statistical Mechanics Principles

Thermodynamic properties of solids are macroscopic quantities which - although based on interactions occurring at the atomic scale - do not necessitate knowing the underlying microscopic interactions. Properties at thermodynamic equilibrium do not change with time, however, fluctuations occur frequently at the atomic scale due to thermal vibrations. Each of the various microstates (σ) a system can sample has an associated energy E_σ. These microstates are dependent on various excitations of the system and include electronic excitations, vibrational excitations and configurational excitations. Each of these energies can be obtained by solving the Schrodinger equation. Statistical mechanics serves as the bridge between these atomic-level fluctuations

and macroscopic bulk properties. The time-independent macroscopic properties are determined through averaging the microstates of the system. The probability that the solid is in a given microstate σ at constant number of atoms (N), temperature (T), and volume (V) is given by

$$P(\sigma) = \frac{1}{Z}\exp(\frac{-E_\sigma}{k_B T}) \tag{2.1}$$

where k_B is the Boltzmann constant and Z is the partition function

$$Z = \sum_\sigma \exp(\frac{-E_\sigma}{k_B T}) \tag{2.2}$$

Equation 2.1 indicates the amount of time the system spends in any particular state with the partition function (Equation 2.2) serving as a normalization factor. The partition function is the sum over each microstate σ oft the exponent of the microstate's energy divided by kT. Additionally, the Gibbs free energy is related to the partition function through

$$G = -k_B T \ln(Z) \tag{2.3}$$

From the free energy, we can connect first principles calculations to macroscopic properties like battery voltages and phase stability. In a one-component system like lithium-ion battery electrodes, the open-circuit voltage is related to the difference in the Li chemical potential (μ_{Li}) between the cathode and anode, according to the Nernst equation:

$$V(x) = -\frac{\mu_{Li} - \mu_{Li}^{ref}}{ze} \tag{2.4}$$

where z is the valence of the intercalating species (1, in the case of Li), e is the charge of an electron, μ_{Li} is the chemical potential of lithium in the cathode Li_xMO_2 and μ_{Li}^{ref} is the chemical potential of lithium in the reference electrode. If we take

metallic lithium to be the reference electrode, then it has constant chemical potential; consequently, the voltage can conveniently be inferred just from examining the phase stability across the composition of the cathode.

The Gibbs free energy is crucial for phase stability predictions, which is determined by examining the relative free energies of various phases at different temperatures. Minimizing the Gibbs free energy yields the thermodynamic equilibrium. To accurately evaluate Equations 2.1-2.3, it is necessary to determine E_σ for all possible microstates in the system. Because the number of microstates is incredibly large, we use a model to extrapolate the first-principles data from a set of calculations to describe any microstate; this is described in further detail in Section 2.2 of this chapter.

2.2 Cluster Expansion Formalism

We use the partition function (2.2) to accurately link macroscopic properties to first principles calculations. However, the number of potential microstates the sum is over is a very large number, which means it is impossible to calculate all possible microstates of a system. During charge and discharge of a Li-ion battery, Li atoms can either randomly or preferentially fill specific, well-defined crystallographic sites, leaving vacancies at the remaining sites. The possibilities of lithium arrangements on structures across a composition range for a cathode scales with 2^N, where N is the number of different sites lithium atoms or vacancies can fill. Clearly, this will explode with complex structures. These configurational excitations are the most important in a lithium-ion battery material, and we use a cluster expansion[29] to drastically reduce the number of configurational microstate first-principles calculations (detailed in Section 2.3) we must perform to garner insight into macroscopic properties. It is convenient to introduce occupation variables, σ_i, that are +1 (-1) if a lithium (vacancy) occupies site i. The vector $\vec{\sigma}$ then defines a given configuration within the

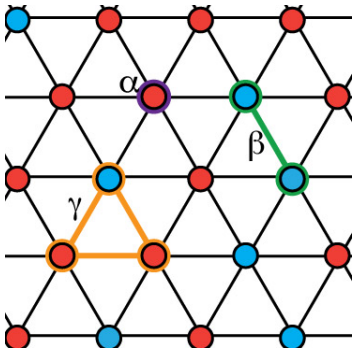

Figure 2.1: Clusters on a two-dimensional triangular lattice. Lithium atoms/vacancies randomly decorate the structure as red/blue circles

host structure as $\vec{\sigma} = (\sigma_1, \sigma_2, ..., \sigma_N)$.

However, it is more useful to classify configurations as *products* of occupation variables, which are grouped into clusters of single sites, pairs, triplets, or quadruplets. These polynomials can be defined as[29]

$$\phi_\alpha(\vec{\sigma}) = \prod_{i \in \alpha} \sigma_i \tag{2.5}$$

where i are the sites that belong to cluster α. Three examples of these types of clusters (one point, α; one pair cluster, β; and one triplet cluster, γ) are shown in Figure 2.1. Depending on what exists (e.g. Li atom or vacancy, with different σ_i values) at each site within the cluster , that polynomial will have a different value.

It can be shown[29] that the set of cluster functions $\phi_\alpha(\vec{\sigma})$ form a complete and orthonormal basis in configuration space which ultimately means that any property that depends on how Li atoms and vacancies are ordered on a lattice can be expanded as a linear combination of these functions. Since energy depends on how atoms are arranged, we can write the energy of any configuration as an expression of clusters

$$E(\vec{\sigma}) = V_0 + \sum_i V_i \sigma_i + \sum_{i,j} V_{i,j} \sigma_i \sigma_j + \sum_{i,j,k} V_{i,j,k} \sigma_i \sigma_j \sigma_k + ... \tag{2.6}$$

where σ are the occupation variables at sites i, j, k and the V are constant coefficients for each cluster and referred to collectively as the effective cluster interactions (ECI). Alternatively, we can write this more broadly as

$$E(\vec{\sigma}) = V_0 + \sum_{\alpha} V_\alpha \phi_\alpha(\vec{\sigma}) \tag{2.7}$$

where α indexes over all clusters.

By calculating a subset of configurational excitations, the ECI can be fit for that particular crystallographic system, and then the energy of any configuration can be reasonably predicted.

2.3 First Principles Calculations

Any electronic structure calculation (like the configurational excitations described in the previous section) begins with the quantum mechanical time-dependent Schrodinger equation given by

$$H\Psi = E\Psi \tag{2.8}$$

where H is the Hamiltonian operator for the system, Ψ is the many-body wave function for a particular fluctuation, and E is the total energy of the solid. Solving this equation directly is computationally incredibly expensive, so it is useful to introduce various approximations which aim to simplify the problem.

Within the Born-Oppenheimer approximation, electrons (with a much smaller mass than the nucleus of an atom) are assumed to instantaneously adjust their state to any change in position of the nuclei (which are treated as fixed). The coordinates of the nuclei now serve only as parameters of the Schrodinger equation, and the

Hamiltonian can be written as

$$H = T + V_{ee} + V_{ne} + V_{nn} \tag{2.9}$$

where the first term T is the kinetic energy operator,

$$T = -\frac{1}{2}\sum_{j} \nabla_j^2 \tag{2.10}$$

The second term, V_{ee} is the potential from the electron-electron interaction and is defined as

$$V_{ee} = \sum_{i}\sum_{j<i} \frac{1}{|\vec{r_j} - \vec{r_i}|} \tag{2.11}$$

where the $\vec{r}$ refer to the positions of the electrons, and the sums over i and j are over all electrons in the solid. The third term in 2.9

$$V_{ne} = \sum_{j} v(\vec{r_j}) \tag{2.12}$$

describes the Coulomb interactions between the nuclei and the electrons of the solid, and the last term

$$V_{nn} = \sum_{n}\sum_{m<n} \frac{Z_m Z_n}{|\vec{R_m} - \vec{R_n}|} \tag{2.13}$$

is the Ewald energy arising from the Coulomb interaction between the nuclei with charge Z. It does not involve the electronic wavefunction Ψ, so is simply additive and can be neglected when solving the eigenvalue equation for the electronic ground state and then added back in to the electronic energy to obtain the total energy of the crystal.

Various approximations are used to simplify solving the many-body Schrodinger equation above. The Hartree method neglects electron-electron repulsion by considering a simpler system of non-interacting electrons, however, in reality electrons are

correlated in that they are repelled by Coulomb interactions from other electrons; a given electron will avoid space occupied by another electron. The Hartree-Fock method [30],[31],[32] fixes this by taking linear combinations of these Hartree products and using a Slater determinant, to introduce the exchange correlation effects from electrons. This approach is still limited to very simple systems usually no larger than molecules.

For larger solids, density functional theory (DFT) [31],[33],[34] comes into play. Hohenberg and Kohn (and extended by Levy) [34],[35] showed that the electron density

$$\rho(\vec{r}) = \langle\psi| \sum_j \delta(\vec{r} - \vec{r}_j)|\psi\rangle \tag{2.14}$$

can determine the ground state energy of a crystal,

$$E[\rho] = F[\rho] + \int \rho(\vec{r})v(\vec{r})d\vec{r} \tag{2.15}$$

In Equation 2.15, $F[\rho]$ is not rigorously known, and instead is separated into

$$F[\rho] = T_s[\rho] + V_H[\rho] + E_{XC}[\rho] \tag{2.16}$$

where both $T_s[\rho]$, the kinetic energy of a system of non-interacting electrons, and $V_H[\rho]$, the Hartree potential arising from electron-electron interactions, are approximations to the comparable contributions of the ground-state energy. The last term is the exchange-correlation energy which includes the difference between the kinetic energies of a system of independent electrons with density ρ and the actual interacting system with the same density. This difference is generally expected to be small[31] and E_{XC} primarily accounts for a correction to $V_H[\rho]$ arising from electron correlations. The exchange-correlation energy is not exactly known, however various means

exist to approximate it.

2.3.1 Local Density and Generalized Gradient Approximations

The local density approximation is the simplest approximation for determining the exchange-correlation energy, $E_{XC}[\rho]$, in Equation 2.16. It assumes that the electron density locally behaves like a homogenous electron gas[36], the properties of which are well-known. Although LDA usually predicts over-binding in systems (i.e. LDA predicts bond lengths that are smaller than those seen experimentally), such as the c-lattice parameter in lithium intercalation materials, for systems where electron densities vary rapidly, LDA performs well. However, in systems where the electron states are highly localized, LDA tends to break down as it is unable to capture the strong correlations between the localized electrons.

The generalized gradient approximation (GGA) is still local like LDA, however it takes the gradient of the electron density into account. Compared to experimental results, GGA tends to predict smaller binding energies and longer bond lengths. Unless otherwise noted, all calculations in this work were performed using GGA as parameterized by Perdew, Burke and Ernzerhof (PBE)[37].

2.3.2 van der Waals Corrections to the Generalized Gradient Approximation

Neither GGA nor LDA take into account the van der Waal's (vdW) interactions that are dominant in between the transition metal layers of intercalation materials. LDA tends to better predict qualitative trends than GGA, however, since LDA also underestimates the bond lengths, the values predicted by LDA are usually much lower than experimentally found. This makes predicting diffusion barriers difficult as migration is known to be very dependent on c-lattice parameter. The difficulty in describing the vdW interactions is that within GGA and LDA, local approxima-

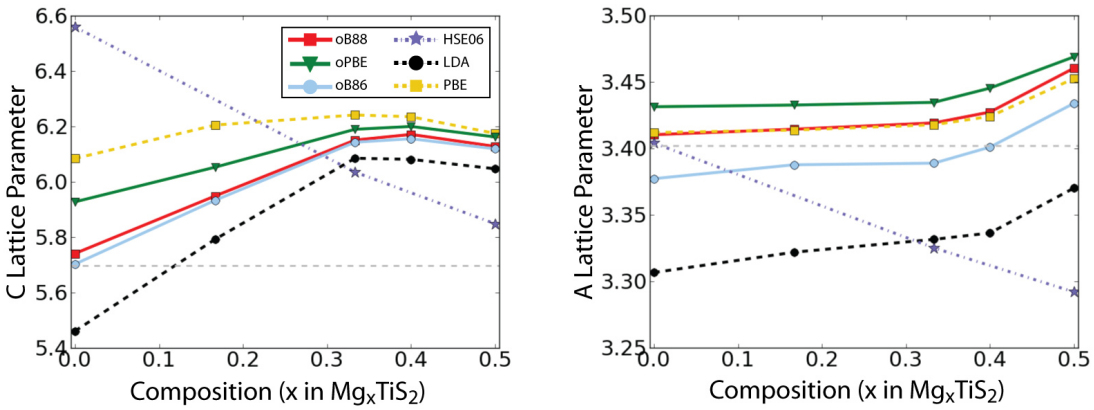

Figure 2.2: Calculated c- and a-lattice parameters for Mg_xTiS_2 (0¡x¡0.5) using different approximations to DFT. Solid lines correspond to PBE with vdW-DF corrections to account for the vdW forces. Dashed lines correspond to LDA (black) and standard PBE (yellow), while the purple dot-dashed line corresponds to HSE06

tions are employed while the vdW interaction is a non-local correlation effect. A variety of different corrections have been introduced to better account for the vdW interactions[38],[39],[40],[41],[42],[43],[44],[45]. These methods have proven reliable for both structural parameters and band gaps for MoS_2 and MoO_3[46], and V_2O_2[47].

In Chapter IV, we evaluate compounds along the composition range TiS_2 to $Mg_{0.5}TiS_2$. A large fraction of binding between adjacent TiS2 slabs in the absence of intercalating species in the layered crystal structures is due to Van der Waals attraction. We applied van der Waals corrections through different exchange functionals using the vdW-DF[45] method: optPBE, optB86, and optB88. To assess the reliability of the various approximations to DFT in describing the properties of Mg_xTiS_2, we compare in Figure 2.2 the a- and c-lattice parameters as a function of Mg concentration for the lowest energy Mg-vacancy orderings within the intercalation layers of the layered form of TiS_2 having an ABAB sulfur stacking sequence. Since migration barriers are very sensitive to the c-lattice parameter in layered intercalation compounds[48],[49], it is essential that the correct dependence of this lattice parameter with concentration is predicted. Figure 2.2 and past studies[48] shows

that LDA, while correctly predicting a contraction of the c-lattice parameter as the number of intercalating species between the layered TiS_2 slabs decreases has a tendency to overbind and quantitatively underpredicts the c-lattice parameter of TiS_2. Nevertheless, LDA has proven very reliable in predicting qualitative trends in layered intercalation compounds, including Li_xTiS_2[48] and $LiCoO_2$[50]. GGA in contrast predicts a c-lattice parameter for TiS_2 that is substantially above the experimental value. HSE has so far also not been proven reliable in accounting for van der Waals interactions[51] and in fact predicts an increase in the c-lattice parameter as the Mg concentration decreases with a value for the c-lattice parameter of TiS_2 that differs from the experimental value by 15%. As is clear in Figure 2.2, the application of van der Waals corrections to GGA based on the vdW-DF[43],[45] method, such as optPBE, optB86 and optB88, results in more accurate predictions of the c-lattice parameter as compared to those predicted with LDA and GGA.

2.3.3 Hybrid Functional Calculations

These calculations combine Hartree-Fock (HF) with Density Functional Theory with the aim of improving the accuracy of the exchange-correlation functional. These calculations are performed by combining fractions of the HF exchange energy and a conventional semi local functional. The exact HF exchange energy cancels the self-interaction error in the electron energy, which helps to reduce the problem of overdelocalized electrons in LDA and GGA.

Hybrid functionals grew first from chemistry with the introduction of the B3LYP functional (as well as its predecessors BHH and BHLYP), which fits some parameters to experimental data. Only recently has the world of hybrid functionals transitioned out of molecular chemistry[52],[53] and into larger systems like transition metal oxides and other materials of interest as new functionals have been introduced that are not specifically tailored to molecular chemistry applications,[54],[55].

The HSE formalism has been shown to be much more successful than GGA in both predicting intercalation potentials for Li-ion battery materials, as well as structural changes upon lithiation[51]. Additionally, and most importantly for this work, HSE functionals have been shown to improve bulk properties like formation enthalpies and band gaps [56]. However, hybrid functionals do not take into account the role of van der Waal's forces, so if this bonding plays a dominant role in the system under investigation, it is important to account for these effects as described in the previous section. As could be expected, by including a portion of the HF energy, these calculations are substantially more expensive, so hybrid calculations tend to be used only when necessary. In this work, the electronic structure of Li_3OCl as well as structures along the composition range TiS_2 to $Mg_{0.5}TiS_2$ were calculated using HSE06.

2.3.4 Shortcomings

Although DFT is quite reliable in predicting thermodynamic properties, in certain cases, due to varying approximations, DFT misses the mark. For example, approximations to DFT reliably under-predict the voltage across an entire composition range. This can be easily accounted for by simply shifting the entire curve calculated with DFT to match that of an experimentally found curve (e.g. matching the computationally predicted voltage at a plateau to the voltage found at the same plateau). Another issue arises examining phase stability with hulls including oxygen gas as an endpoint (e.g. in this thesis, Chapter III looks at configurations within the Li-O-Cl composition space). It is well-known that both GGA and LDA poorly determine the binding energy of the O_2 molecule; this error is not necessarily cancelled when forming an oxide that is bonded electrostatically (e.g. this could arise in Li_3OCl which is ionic). This results in oxidation energies calculated with the GGA and LDA approximations to DFT that are less negative than experimental values. It's possible to then

shift the energy of oxygen for calculating a hull to be more representative of what is occurring experimentally. However, the nature of the bonding changes the value of the shift. This has been rigorously described for transition metal oxides[57], however, determining shifts for materials which have different types of oxygen bonding for different compounds along a phase line (e.g. Li_2O_2 vs. Li_2O within the Li-O system) is similar to comparing apples to oranges - the same shift will not suffice for both scenarios which exhibit different oxygen bonding. With this in mind, it is important to realize where errors could originate within a given system.

CHAPTER III

Solid Electrolyte Li_3OX (X=Cl,Br)

We investigate phase stability and ionic transport mechanisms in two recently discovered superionic conductors. These compounds, which have an anti-perovskite crystal structure, have potential applications as solid electrolytes in Li-ion batteries to replace the currently-employed liquid electrolytes. We identify a low-barrier three-atom hop mechanism involving Li interstitial dumbbells. This hop mechanism is facile within the (001) crystallographic planes of the perovskite crystal structure and is evidence for the occurrence of concerted motion, similar to ionic transport in other solid electrolytes. Our first-principles analysis of phase stability predicts that antiperovskite Li_3OCl (Li_3OBr) is metastable relative to Li_2O and LiCl (LiBr) at room temperature. We also find that while the band gap of Li_3OCl exceeds 5 eV, the metastable antiperovskite becomes susceptible to decomposition into Li_2O_2, LiCl and $LiClO_4$ above an applied voltage of 2.5 V, suggesting that these compounds are most suited for low-voltage Li batteries provided the formation of Li_2O can be suppressed. This work has been published in Chemistry of Materials, an American Chemical Society journal.

3.1 Introduction

Most lithium-ion batteries in use today utilize a liquid electrolyte. While exhibiting high ionic mobilities, liquid electrolytes suffer from a variety of drawbacks[1] that include the off-gassing of polymer solvents, safety concerns prohibiting the use of metallic lithium as the anode, and a narrow electrochemical stability window, which can lead to the decomposition of the electrolyte in what is commonly referred to as the solid electrolyte interphase (SEI) layer. One promising class of solid electrolyte materials for Li-ion batteries are the recently discovered anti-perovskites such as Li_3OCl and Li_3OBr.[12] This class of solid electrolytes exhibit Li conductivities on the order of 1 mScm$^-$1, with a maximum conductivity of 1.94 mScm$^-$1 achieved for a solid solution mixture of Li_3OCl and Li_3OBr.[12]. Unlike either LGPS or other solid electrolytes based on the lanthanide series[58], which have a large number of vacant sites for Li+ diffusion, the antiperovskite structure of Li_3OX (shown in Figure 3.1) does not seem to have high concentrations of transport mediating defects or disorder. There are many compounds with the perovskite structure that exhibit a high ionic conductivity, yet the structures which exhibit the best conductivity tend to be disordered, rather than ordered. Ag_3SI, for instance, has poor conductivity in the antiperovskite structure, but when the S and I ions are disordered, the conductivity in-creases by nearly two orders of magnitude[59],[60]. This is also true for the fluorine-conducting perovksite $RbPbF_3$[61]. Another fluorine-conducting perovskite, $KCaF_3$, exhibits high F- mobility in the orthorhombic structure [62]. $CsPbF_3$ is believed to have high conductivity due to fluorine vacancy diffusion arising from monovalent cation defects that introduce lattice vacancies elsewhere.[63] Li_3OX is unique in that the immobile O and Cl ions remain highly ordered but it still exhibits a high Li+ conductivity at low temperatures.[12]. With this unique structural characteristic in mind, we explore phase stability and Li transport mechanisms in this new class of anti-perovskite solid electrolytes having stoichiometry Li_3OX (X=Cl, Br)[12]. We

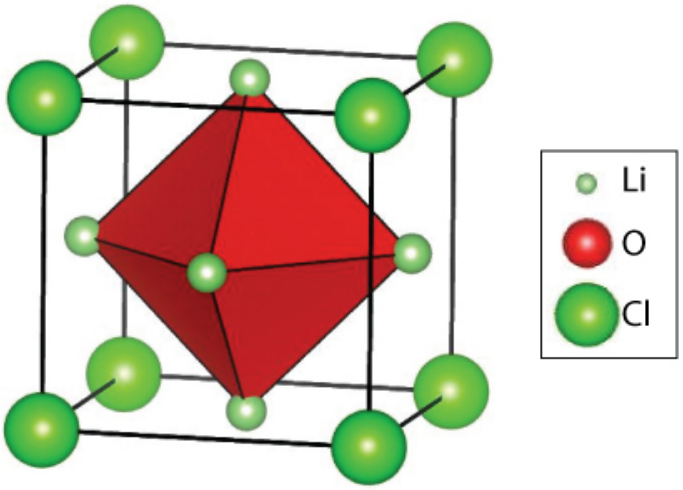

Figure 3.1: Li_3OCl with the antiperovskite crystal structure. Li occupy the face-centered sites, O occupies the body-centered site, and Cl occupy corner sites.

find that the Li_3OCl (Li_3OBr) anti-perovskites are meta-stable phases at 0K relative to decomposition into LiCl (LiBr) and Li_2O, as was predicted by Zhang et al[11]. When considering phase stability in the absence of Li_2O (valid in cases where it is kinetically difficult to form), we find not only Li_3OCl (Li_3OBr) to be stable, but also a variety of LiCl (LiBr) deficient Li_3OCl (Li_3OBr) phases. Finally, our analysis of Li transport mechanisms has shown the existence of a fast conduction mechanism involving a dumbbell interstitial, which is similar to the mechanism discovered through MD simulations on the fluorine superionic perovskite, $KCaF_3$[62].

3.2 Phase Stability

Examining phase stability allows us to determine if materials have the capabilities to be implemented as a solid electrolyte in a battery system. If the material is only metastable or is likely to decompose, it will be more difficult to both synthesize and use in a battery. Also, because the electrolyte will be cycled over a voltage window, it is important to examine the stability relative to both the chemical potential of Li and electrons in addition to the thermodynamic phase stability. We examined

phase stability within the Li-O-X (X=Cl, Br) ternary spaces as well as along the Li_3OCl-Li_3OBr pseudo binary. We calculated the electronic band structure to serve as a maximum theoretical window for the voltage stability and we also calculated a grand canonical phase diagram which allows for the determination of phases present at various points of charge.

3.2.1 Phase Stability in the Li-Cl-O & Li-Br-O Composition Space

We investigated the thermodynamic stability of Li_3OCl by calculating the energies of all known and likely phases in the Li-Cl-O ternary composition space. Our global phase stability analysis indicated that we can restrict ourselves to the Li-LiCl-Li_2O_2 composition triangle containing the Li_3OCl composition.

Known phases in this composition space include bcc Li, rocksalt LiCl, Li_2O, Li_2O_2, Li_5OCl [4][64],and the recently synthesized anti-perovskite Li_3OCl phase[12]. To supplement this list of candidate phases, we also enumerated derivative structures of the anti-perovskite Li_3OCl phase. We primarily considered configurational and compositional perturbations to the anti-perovskite crystal structure that preserve charge neutrality assuming formal ionic valences of +1 for Li, -1 for Cl, and -2 for O. Accordingly, lithium vacancies in the anti-perovskite crystal structure can be created in two ways: (i) either by removing a Cl ion for each Li vacancy (i.e., a LiCl vacancy) or (ii) by removing an oxygen ion for every two Li vacancies (a Li_2O vacancy).

The lowest-energy compounds with charge neutral Li_2O vacancies had slightly positive mixing energies relative to Li_2O and LiCl ranging from 37 meV/atom - 48 meV/atom. Low-energy structures with LiCl vacancies had mixing energies ranging from 46meV/atom 86 meV/atom. We calculated the energies of 374 symmetrically distinct configurations of these types. We also calculated energies of 174 configurations at compositions that deviate from the Li_2O-LiCl line of charge-neutral composi-

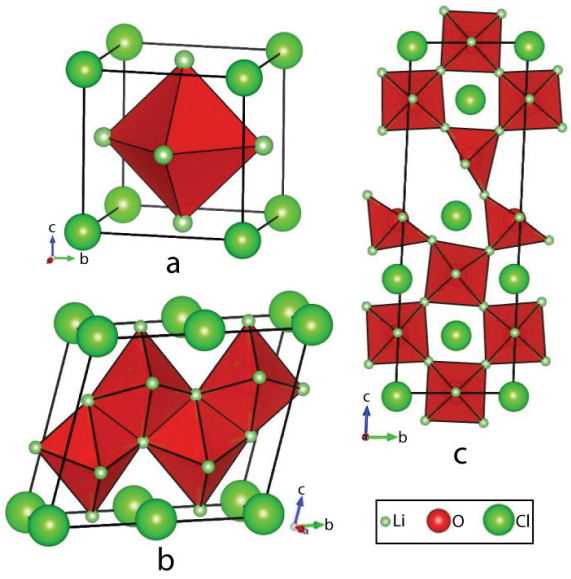

Figure 3.2: a) Defect-free Li_3OCl (reprinted to show differences between this structure and (b) and (c). b) Stable Li_5O_2Cl structure. The oxygen octahedra distort to allow for corner sharing of lithium atoms because of the two LiCl vacancies present in this supercell. c) Stable $Li_{17}O_6Cl_5$ structure. The structure distorts slightly to compensate for the LiCl vacancy.

tions. The lowest energy configurations in this subset are within the Li_2O-LiCl-Li_2O_2 triangle of composition space (shown in Figure 3.2) and have mixing energies relative to Li_2O, LiCl and Li_2O_2 that range from 113meV/atom to 252meV/atom. These substantially higher mixing energies for non-charge neutral compounds indicate that only structures with charge-neutral variations (i.e., along the Li_2O-LiCl line in composition space) are candidates that could possibly be synthesized.

Qualitative predictions of phase stability in the ternary Li-Cl-O and Li-Br-O composition spaces are sensitive to the relative accuracy of the formation energies of the various phases competing for stability. Systematic errors in DFT formation energies usually cancel when comparing phases that have similar bonding and structure. Corrections have been established to remove systematic DFT errors when comparing energies of very different states of matter, such as reactions involving molecular oxygen and crystalline oxides[57]. Bonding in the compounds appearing in the Li-Cl-O and Li-Br-O ternaries changes qualitatively with concentration and error cancelation

among DFT formation energies may not occur. Bonding in the Li_2O oxide, for example, differs from that in the Li_2O2 peroxide. Recently Kang et al[65] introduced a scheme to remove systematic DFT (and DFT+HSE) errors based on experimentally measured oxide and peroxide formation energies and showed that the correction needed for oxides differs from that needed for peroxides. In this work, we have not attempted to correct for DFT errors between oxides and peroxides. However, we realize that correcting for these errors by using empirical shifts may alter relative stability compared to that predicted here. A difficulty posed by this approach of correctional shifts is the ambiguity that emerges for phases with oxygen bonding that do not clearly fall into a well-defined class for which corrections have been established. An important example in the Li-Cl-O ternary is the $LiClO_4$ phase in which bonding is likely to differ substantially from that in oxides and peroxides (which have established shifts). Using DFT-PBE, we find three phase regions between LiCl, Li_2O and Li_2O_2, but corrections to the Li_2O and Li_2O_2 formation energies as proposed by Kang et al[65] may result in three phase regions between LiCl, Li_2O and $LiClO_4$ as well as between Li_2O, Li_2O_2 and $LiClO_4$ depending on the type of corrections that are applied to the formation energy of $LiClO_4$. This qualitative difference in predicted phase stability in the Li-Cl-O ternary, however, should not affect our predictions about (i) the metastability of antiperovskite Li_3OCl and Li_3OBr at zero Kelvin and its stability at high temperature, (ii) the hierarchy of charge neutral defect formation energies (discussed in more detail later in this chapter) and (iii) the Li migration mechanisms and barriers since these results are all based on energy differences between phases with very similar bonding (also discussed in detail later in this chapter). Furthermore, it should not alter the prediction that even if decomposition of Li_3OCl into LiCl and Li_2O is suppressed, it still becomes susceptible to decomposition at relatively low voltages (2.5V) into phases having lower Li concentration. If phase stability in the ternary Li-Cl-O composition space is altered when including bond

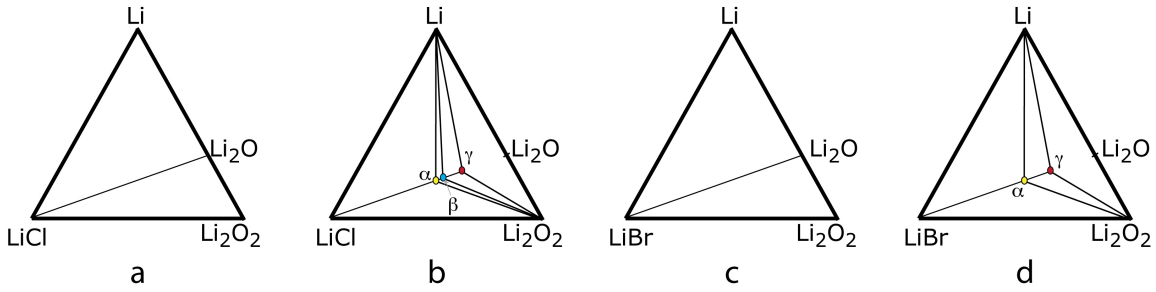

Figure 3.3: Calculated LiCl-Li-Li_2O_2 and LiBr-Li-Li_2O_2 phase diagrams. a) Stable LiCl-Li-Li_2O_2 phase diagram. b) metastable LiCl-Li-Li_2O_2 phase diagram assuming kinetic suppression of Li_2O formation. Three new phases become stable: α, Li_3OCl; β $Li_17O_6Cl_5$; γ Li_5O_2Cl. c) Stable LiBr-Li-Li_2O_2 phase diagram. d) Meta-stable LiBr-Li-Li_2O_2 phase diagram assuming kinetic suppression of Li_2O. Li_3OBr and Li_5O_2Br (γ) are stable.

specific corrections, the decomposition products when examining a voltage window range may include $LiClO_4$ as well.

Figure 3.3 shows the calculated ternary phase diagram in the Li-LiCl-LiO_2O_2 composition triangle at zero Kelvin. The anti-perovskite Li_3OCl is not predicted to be thermodynamically stable at low temperature. In thermodynamic equilibrium, the anti-perovskite Li_3OCl phase, which has a composition along the LiCl-Li_2O tie line, will therefore decompose into a two-phase mixture of LiCl and Li_2O. The change in energy per atom for this decomposition is 22 meV. This result is consistent with similar predictions by Zhang et al.[11] The Li_5OCl_3 phase[64] is also not predicted to be stable and is also susceptible to decomposition into LiCl and Li_2O with a reaction energy of 136 meV per atom.

We also calculated a metastable phase diagram in the absence of Li_2O, Figure 3.3b. This meta-stable 0K phase diagram can be viewed as valid when sluggish kinetics prevents the formation of Li_2O. Evidence from research on Li-air batteries suggests that Li_2O is difficult to form electrochemically[66]. The meta-stable phase diagram of Figure 3.3b shows not only perovskite Li_3OCl but two additional anti-perovskite derived structures having stoichiometries of $Li_{17}O_6Cl_5$ and Li_5O_4Cl. The first of

these, $Li_{17}O_6Cl_5$, which can be derived from anti-perovskite Li_3OCl by removing a LiCl unit and thereby introducing a Li and Cl vacancy to a supercell containing six anti-perovskite unit cells, belongs to space group Pm (#6). Li_5O_2Cl. can be derived from Li_3OCl by removing two LiCl units to a supercell consisting of four anti-perovskite unit cells. This structure also belongs to space group Pm (#6). The fully relaxed crystal structures of $Li_{17}O_6Cl_5$ and Li_5O_2Cl are illustrated in Figure 3.2 and their Wyckoff positions can be found in Appendix 1.

We also constructed a Li-O-Br phase diagram by calculating the energies of the same structures as those used for the Li-O-Cl analysis, replacing the Cl with Br. While the existence of $Li_7O_2Br_3$ has been reported[67], no structural data is available to enable a calculation of its formation energy. Similar to Li_3OCl, the anti-perovskite Li_3OBr is only stable if Li_2O is kinetically prevented from forming, as is evident from a comparison of the equilibrium and meta-stable phase diagrams, Figures 3.3c and 3.3d. Only one additional anti-perovskite derived phase appears in the metastable phase diagram Figure 3.3d, having stoichiometry Li_5O_2Br. The atoms occupy equivalent positions as Li_5O_2Cl, Figure 3.2c, and the lattice parameters are slightly larger than Li_5O_2Cl.

Because Li_3OCl is predicted to be unstable at 0K, we also used density functional perturbation theory to determine if it becomes stable at elevated temperatures. We calculated the phonon band structure (shown in Figure 3.4a using the equilibrium 0K volumes and fitting force constants to small perturbations. We find that there are imaginary frequencies at both the R and the M k-points, which points to mechanical instability. Perovskite structures are known to have a variety of polymorphs, one classification of which is rotations of the octahedra (in the case of Li_3OCl, the lithium atoms will shift slightly off center of their positions yet still remain coordinated six-fold with oxygen); these have been heavily studied, and the classification system is based on work of Glazer, et al[68]. These different distortions (two of which are shown

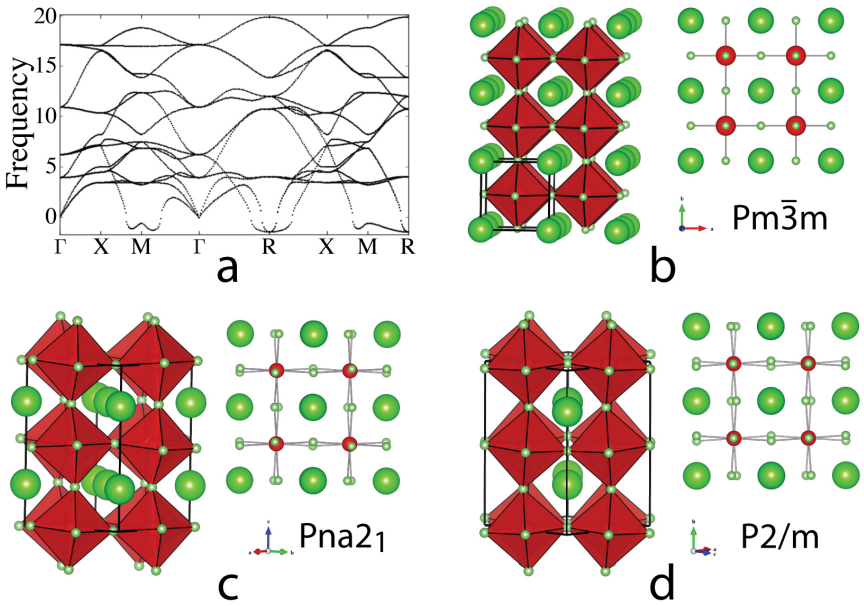

Figure 3.4: Different polymorphs of Li_3OCl with unit cells shown in black boxes. a) phonon band structure of cubic $Fm\bar{3}m$ Li_3OCl. b) 2x2x3 supercell of cubic Li_3OCl. c) low-energy polymorph structure $Pna2_1$ with octahedral tilts in all three directions. d) lowest-energy polymorph structure P2/m with octahedral tilts in two directions.

in Figure 3.4b and 3.4c) can stabilize different phonon modes, so we then calculated eighteen structures which are known to exist for other perovskite structures and determined equilibrium 0K atomic positions for Li_3OCl. We find that cubic Li_3OCl is not the lowest energy structure at 0K; however, nearly all the distortions are within 2meV per formula unit of each other. This indicates that the energy landscape of Li_3OCl should be very flat as there is no single structure which is clearly preferred at low temperatures. Ivy Chen in the Van der Ven group is currently investigating this further.

3.2.2 Electronic Structure

A crucial property of electrolytes is that they are not electronically conducting. The band gap of a solid electrolyte must therefore be at least as large as the voltage range of the battery. Figure 3.5 shows the HSE06 band structures of Li_3OCl and

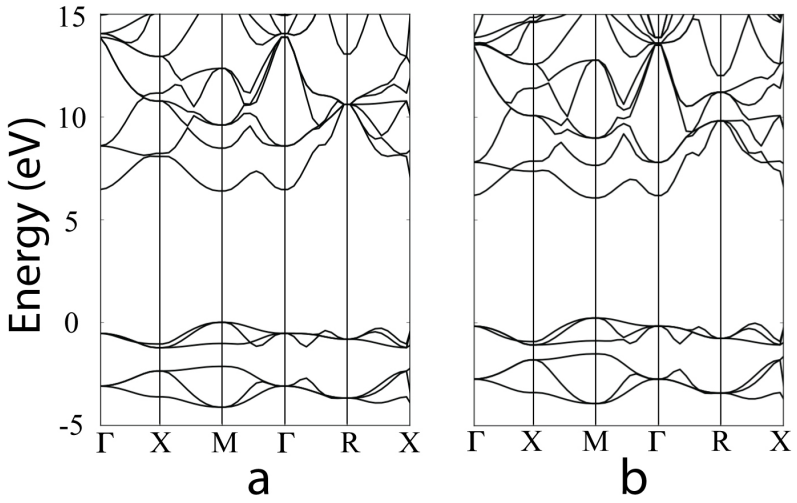

Figure 3.5: Electronic Band Diagram of a) Li_3OCl and b) Li_3OBr calculating using HSE06 hybrid pseudopotential

Li_3OBr. Both materials have direct band gaps, and the conduction and valence band extrema are located at the M point of the first Brillouin zone. The band-gap values are 6.39eV and 5.84eV for Li_3OCl and Li_3OBr, respectively. Both of these band gaps are large which, although not a precise measure for electrochemical s tability, does provide an upper limit for the electrochemically stable region[2]. High voltage cathodes operate at 4V, so a band gap larger than 5eV is suitable for use in lithium-ion batteries

3.2.3 Phase Stability as a Function of Lithium Chemical Potential (μ)

Electrolytes must be stable over a wide interval of Li chemical potential values[8]. Due to the high mobility of Li ions in a Li battery, local changes in composition can easily be achieved if such changes are thermodynamically preferred. Since the solid electrolyte separates the anode from the cathode, it is in contact with two Li reservoirs: one at high Li chemical potential (the anode, metallic Li in the case of a solid electrolyte or more commonly, graphite) and the other at low Li chemical potential (the cathode, commonly a transition-metal oxide like $LiCoO_2$). The voltage of a Li battery is determined through the Nernst equation by the difference in Li chemical

potential (μ_{Li}) between the anode and the cathode (V=-(μ_{Li} - μ^o_{Li}). Therefore, the higher the voltage of the Li battery, the larger the Li chemical potential interval within which the electrolyte must be stable. Phase stability at constant Li chemical potential can be conveniently analyzed by minimizing a grand canonical potential as defined by Ong et al[69]. This shows the voltage range at which the material in question is thermodynamically stable. Figure 3.6 shows a calculated Li-chemical potential versus oxygen concentration phase diagram as obtained by minimizing the Li grand canonical potential. The lithium chemical potential reference state is metallic lithium. The phase diagram was calculated in the absence of Li_2O, since, as described above, Li_3OCl is not stable with respect to decomposition into Li_2O and LiCl. The phase diagram therefore reflects metastable equilibrium valid under conditions where Li_2O is kinetically suppressed from forming. Considering the difficulty in forming Li_2O electro-chemically in Li-air batteries, this phase diagram can serve as a map of possible decomposition products when Li_3OCl is used as an electrolyte. The composition axis corresponds to the fraction of oxygen relative to the amount of oxygen and chlorine present. Since the phase diagram is valid at constant Li chemical potential, the Li concentration is not constant over the various phases appearing in the phase diagram.

This phase diagram can be interpreted in a similar way as a temperature-composition phase diagram, the difference being that the vertical axis is the negative of the Li chemical potential (relative to metallic Li, thereby making it equal to the voltage of the battery) instead of the temperature. Vertical lines in the phase diagram correspond to stable line compounds, while all the horizontal lines correspond to triple points (similar to eutectoids or peritectoids in a temperature-composition phase diagram). The large empty regions between horizontal and vertical lines in the phase diagram denote two-phase coexistence. The phase diagram indicates that an electrolyte with a stoichiometric ratio of O and Cl will be thermodynamically stable

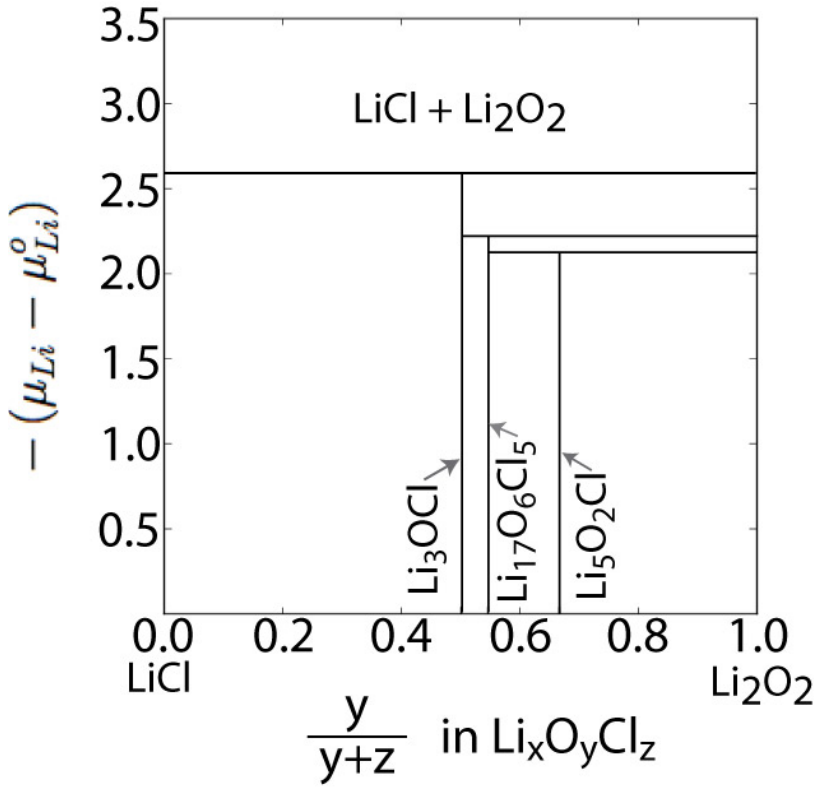

Figure 3.6: Oxygen/Chlorine composition versus Li chemical potential phase diagram calculated assuming suppression of Li_3OCl decomposition into LiCl and Li_2O. Metastable Li_3OCl can resist decomposition up to an applied voltage (relative to metallic Li) of 2.55V whereas the two other stable Li_2O-rich phases will decompose at lower voltages around 2.1V. LiO_4Cl appears above 2.92V.

in the perovskite Li_3OCl phase (provided decomposition into Li_2O and LiCl is suppressed) for voltages up to 2.55 eV. Above that voltage, Li_3OCl will decompose into Li_2O2 and LiCl. The other metastable perovskite derivatives ($Li_{17}O_6Cl_5$ and Li_5O_2Cl) are stable at higher oxygen to chlorine ratios, but decompose at slightly lower voltages than the perovskite Li_3OCl phase, so these compounds should not be present in an SEI-type layer. This is different from LGPS which decomposes into $Li_xP_yS_z$-type derivatives[2] (which exhibit good ionic conductivity) before decomposing into the insulator Li_2S. For Li_3OCl, the off-stoichiometric perovskite derivatives will not form at any point of charge or discharge if the starting electrolyte is perfectly stoichiometric. Additional electrolyte decomposition reactions involving species from the electrodes other than Li are also possible and may occur at voltages even lower than 2.55 eV. These reactions, however, will depend on the chemistry of the electrodes and are not considered in this work. In addition, whether or not the electrolyte decomposes depends on kinetic factors, as de-composition of a single phase into several new phases requires spatial redistribution not only of Li, but also of O and Cl. Furthermore, redistribution may also require electron transport, which could be inhibited if any of the phases are electronically insulating.

3.3 Conductivity

Conductivity is related to both the number of charge carriers as well as the mobility of these carriers. In Li_3OCl, the lack of vacant sites points to a very low number of intrinsic charge carriers, so the majority of charge carriers must come from defects. Examining diffusion pathways enables us to make a prediction of how mobile the Li ions will be in this compound. The product of these values is related to the ionic conductivity.

3.3.1 Charge Carriers: Finding Defects

Solid electrolytes with high Li conductivities tend to have substantial disorder and high vacancy concentrations due to incomplete filling of particular crystallographic sites[7],[9]. The anti-perovskite Li_3OCl and Li_3OBr phases, in contrast, consist of highly ordered Li sublattices. Li migration is there-fore presumably mediated by defects. The simplest defects include Li vacancies and Li interstitials. We investigated formation energies and geometries of vacancy and interstitial defects using the supercell method.

Since Li_3OCl is an ionic material, isolated vacancies and interstitials are likely charged within Li_3OCl. Formation energies of charged interstitials and vacancies therefore depend not only on the Li chemical potential of the Li reservoir from which the excess Li is drawn, but also on the Fermi level of the solid (i.e., the electron chemical potential). The Fermi level is determined by other defects and dopants in the solid as well as the electrodes in contact with the electrolyte. Although this is important to analyze for a full battery system, here we focus on only Li_3OCl. We investigate the energetics of forming charge-neutral defect pairs, with a particular focus on Frenkel defects, which forms when a Li atom from an octahedron moves to an interstitial site, leaving behind a vacancy.

Our supercell calculations with an interstitial Li predict the stability of an interstitial dumbbell (split interstitial) as illustrated in Figure 3.7. Instead of residing in the open space halfway between pairs of Cl ions for example, the excess Li prefers to form a dumbbell configuration with a Li of an octahedron. The center of the dumbbell resides at the octahedron corner of the displaced Li ion. The stable orientations of the Li dumbbell are parallel to the cubic axes of the perovskite crystal.

The Frenkel pair is overall charge neutral; however, there is some charge redistribution, and the vacancy adopts an effective negative charge while the interstitial Li

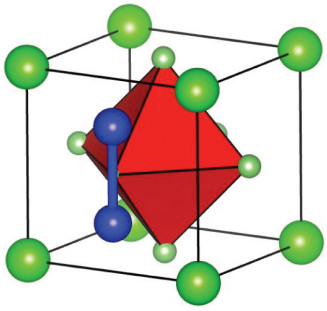

Figure 3.7: Energetically stable Li dumbbell interstitial (split interstitial). An interstitial prefers to split a Li site of an Li_6O octahedron effectively sharing the site (two blue atoms). It resides in the face shared with the four chlorine corner atoms. The dumbbell has two symmetrically equivalent stable orientations parallel to the axes of the anti-perovskite cubic unit cell

has an effective positive charge. Removal of a Li from an octahedron corner introduces a hole in the oxygen p states, located near the top of the valence band. In contrast, the introduction of a Li interstitial (e.g., as an interstitial dumbbell) fills a state at the bottom of the conduction band. In a Frenkel defect, the crystal remains overall charge neutral. However, the electron associated with Li in the conduction band can lower its energy by occupying the empty oxygen p orbitals that are localized around the vacant Li site. The interstitial Li therefore adopts an effective positive charge and the Li vacancy has an excess negative charge. We estimate the formation energy of Frenkel defects by performing DFT calculations using supercells of Li_3OCl. Because vacancies and interstitial Li in Li_3OCl locally have excess charge relative to the perfect crystal, even a charge-neutral Frenkel defect will still form an electric dipole moment. Hence electrostatic dipole-dipole interactions as well as elastic interactions between periodic images of Frenkel defects scale with supercell size. We analyzed the effect of supercell size using three cubic supercells of the Li_3OCl anti-perovskite unit cell: a 3x3x3 supercell having a lattice parameter a = 11.7Å(135 atoms), a 4x4x4 supercell with a=15.6Å(320 atoms), and a 6x6x6 supercell with a=23.4Å(1080 atoms). The Frenkel defect formation energies we calculated are consistent with the Makov-Payne

supercell screening analysis[70], where defect formation energies scale with a $1/a^3$ dependence on the cubic supercell lattice parameter a. Extrapolating our empirically established scaling law, we estimate the Frenkel defect formation energy calculated in a 3x3x3 supercell (6x6x6 super-cell) to differ from the infinite sized supercell crystal by 50 meV (5 meV). The Frenkel formation energy within a 6x6x6 super-cell is predicted to be 1.94eV. This value is large and suggests that only a small fraction of Li vacancies and interstitial dumbbells will be thermally generated. The remarkably low migration barrier for the interstitial dumbbell suggests that high conductivities can be achieved in antiperovskite Li_3OCl and Li_3OBr if high concentrations of Li interstitials are present. The formation energy for Frenkel defects, however, is very high and substantial numbers of Li interstitials are unlikely to be generated through thermal excitation of Frenkel pairs. Other charge-neutral defects can be envisioned by deviating from the ideal anti-perovskite stoichiometry.

Besides Frenkel defects, we also looked at formation energies relative to LiCl and Li_2O for off-stoichiometric compounds. These mixing energies for off-stoichiometric Li_3OCl achieved by introducing charge-neutral defects along the Li_2O - LiCl composition axis are shown in Figure 3.3.1. The mixing energies are calculated relative to the energy of Li_2O and LiCl and are normalized by the number of Li_2O and LiCl units. By comparing mixing energies for off-stoichiometric anti-perovskite at constant concentration it is possible to identify a qualitative hierarchy of the energetic cost of achieving off-stoichiometry through different types of charge-neutral defects. Since Li_3OCl is metastable relative to decomposition in to Li_2O and LiCl, it has a positive mixing energy. Introducing charge-neutral defects to antiperovskite Li_3OCl along the Li_2O-LiCl composition axis results in a further increase in the mixing energy. We considered three classes of charge-neutral defects in variously sized supercells of the anti-perovskite crystal structure to achieve different degrees of off-stoichiometry from ideal Li_3OCl : (i) Li_2O or LiCl interstitials (ii) Li_2O or LiCl vacancies and (iii)

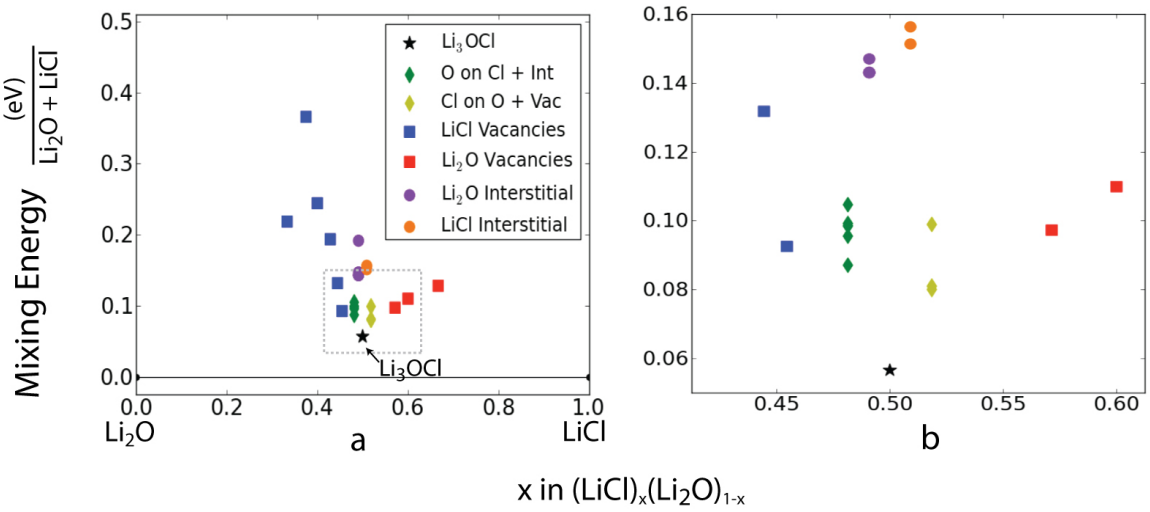

Figure 3.8: Mixing energies of off-stoichiometric antiperovskite derived phases. (a) shows various ways of deviating from the ideal anti-perovskite Li_3OCl stoichiometry from the range Li_2O (x=0) to LiCl (x=1). (b) is an enlarged portion of the gray box in (a). Substitutions on the O/Cl sub lattices, interstitials, and vacancies are denoted by diamonds, circles, and squares, respectively. Li_2O-rich structures have compositions $x < 0.50$ and LiCl-rich structures have compositions with x>0.50. Substitutions on the halogen sublattice have the lowest mixing energies. The defect-free antiperovskite is shown as a black star.

substitutional exchanges of Cl (O) by O (Cl) coupled with the introduction of a Li interstitial (vacancy). The nature of the defect and size of the supercell determines the degree of off-stoichiometry (shown as the composition on the x-axis). Li vacancies, introduced by simultaneously creating either Cl vacancies or O vacancies, were systematically explored with the cluster expansion approach as part of our analysis of phase stability of the anti-perovskite crystal structure. The least energetically costly of these structures are shown as blue and red squares in Figure 3.3.1. Of all the charge-neutral defects considered, these have the lowest positive mixing energies. Li interstitials (vacancies) coupled with substitutional exchanges of Cl (O) by O (Cl) also have low mixing energy penalties relative to the other defect types considered. These are shown as green (yellow) diamonds in Fig. 10. These mixing energies were calculated within a 3x3x3 supercell and by considering varying distances between the Li defect and substituted anion. The least energetically costly structures were those with the shortest distance between the Li defect and anion substitution (1.9 for the extra Cl and Li vacancy and 3.3 for the extra O and dumbbell pair). The highest mixing energies occur for combined cation and anion interstitials (i.e., the simultaneous introduction of a Li interstitial and a Cl interstitial, or two Li interstitials with an oxygen interstitial). This is most likely due to the crystal having to accommodate an extra two (LiCl interstitial) or three (Li_2O interstitial) atoms. Both scenarios were calculated at different distances between the anion interstitial and lithium interstitial(s) in a 3x3x3 supercell. For both LiCl and Li_2O interstitials, the lowest energy is when the interstitials are placed next to each other. LiCl interstitials have higher formation energies than Li_2O interstitials, presumably because of the larger size of Cl. Both the Frenkel defects we investigated as well as other manipulations to ideal stoichiometry have high formation energies. Based on these results, it is therefore not clear how the high conductivity values achieved experimentally using inert gold electrodes[12] are realized at the atomic scale. One possibility is that ex-

cess interstitial Li ions and/or vacancies are introduced during synthesis resulting in slight deviations from ideal Li_3OCl stoichiometry. On the Li_2O-rich (LiCl-rich) side of Li_3OCl, LiCl (Li_2O) vacancies and substitutional replacement of Cl by O (O by Cl) coupled with a lithium interstitial (vacancy) constitute the least energetically costly charge-neutral defects. Synthesis at high temperature and under Li_2O-rich conditions could be a pathway with which Li interstitials are introduced through thermal excitation. The excess Li, which will form interstitial dumbbells, could then participate in ion conduction. Another way to potentially increase conductivity is by substitution on the Li sublattice. The number of Li vacancies can be increased through doping with a 2+ metal (i.e., Mg). By introducing a Mg atom at a Li site, a Li vacancy must be created elsewhere which would facilitate vacancy diffusion. Although vacancies are not as mobile as interstitial Li, a high concentration of vacancies may enable completely different migration mechanisms that take advantage of a large fraction of unoccupied sites as in other solid electrolyte materials. Apart from manipulating the composition of the electrolyte itself, other sources of diffusion-mediating defects could exist by changing the surroundings of the electrolyte (i.e., non-inert electrodes versus inert gold electrodes). When Li_3OCl is placed between an anode and a cathode in a Li battery, the Li interstitial concentration in Li_3OCl, for example, should increase at the interface between Li_3OCl and the metallic lithium anode where the Li chemical potential is high. Li from the metal anode will enter Li_3OCl to lower its chemical potential. However, since Li_3OCl is electronically insulating, the Li will shed its electron, leaving it behind in the metal anode at the electrolyte/electrode interface. The excess Li that has entered Li3OCl is thus positively charged. Similar processes occur at the cathode side (likely then involving charged Li vacancies in Li_3OCl).

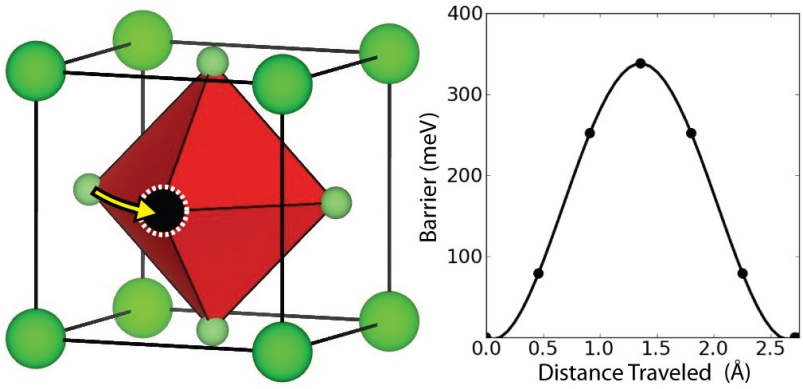

Figure 3.9: Lithium migration around the edge of a Li_6O octahedron into a vacant site (black with dotted white line). The barrier ranges from 310 meV to 380 meV for neutral and charged vacancies in Li_3OCl and Li_3OBr

3.3.2 Diffusion Pathways

We calculated Li migration barriers for both a vacancy diffusion mechanism and an interstitial-dumbbell diffusion mechanism within a 3x3x3 supercell (135 atoms). We also calculated three Li interstitial-dumbbell migration barriers in a solid solution of $Li_3OCl_{0.5}Br_{0.5}$ having Cl-Br disorder as sampled with Monte Carlo simulations. Migration barriers were calculated for either an isolated vacancy or an isolated interstitial dumbbell (i.e., the two components of a Frenkel defect). The barriers were calculated in both charge-neutral and charged cells. The state of charge has little effect on the migration barriers causing it to vary by at most 30 meV.

Figure 3.9 illustrates Li migration into a vacancy, which proceeds along the edge of an oxygen octahedron and has an energy barrier of 340meV (310 meV for a negatively charged vacancy) in Li_3OCl and a barrier of 375meV (370 meV for a charged vacancy) in Li_3OBr. This hop follows a slightly curved path around the oxygen octahedron. Although this is a low barrier, it is still too high to explain superionic conduction. These results com-pare well with previously published vacancy migration barriers of 367meV (405meV) as calculated in smaller 2x2x2 super-cells of Li_3OCl (Li_3OBr)[11].

For the migration of an interstitial dumbbell, we found a low-energy pathway involving a coordinated three-atom move, as illustrated in Figure 3.10. As one Li of

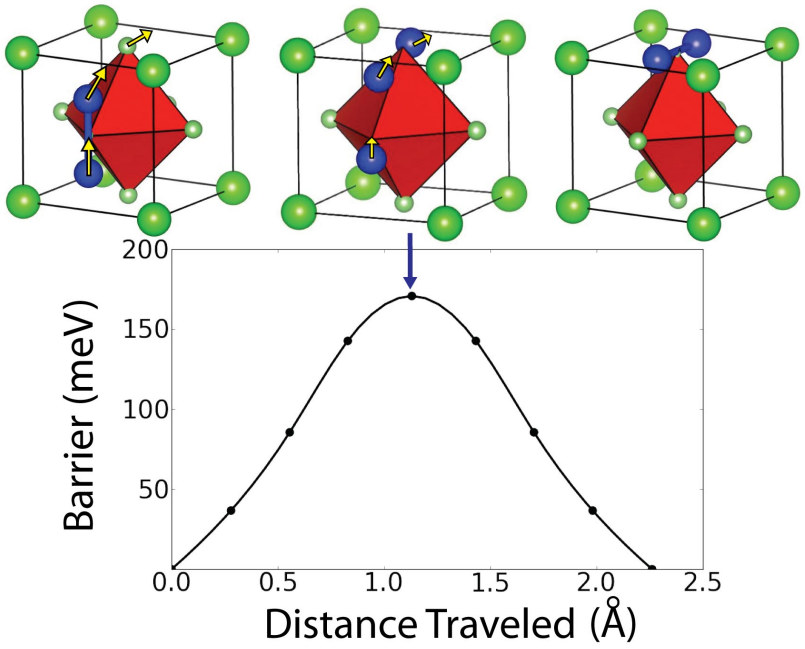

Figure 3.10: Low-barrier migration pathway for a neutral Li split interstitial in Li_3OCl. The barriers range from 145 meV to 175 meV depending on the charge state of the interstitial (neutral or +1) and host material (Li_3OCl or Li_3OBr

a dumbbell pair shifts into an ideal octahedral site (located at a corner of a Li6O octahedron), the second Li of the dumbbell then shifts towards a neighboring lithium site, forming a new dumbbell centered at the original position of the neighboring lithium atom. This hop mechanism keeps the orientation of the dumbbell restricted to a fixed (001) plane of the cubic crystal. The barrier for this hop is only 170 meV (145 meV for a charged interstitial) in Li_3OCl and only 175 meV in Li_3OBr (170 meV for a charged interstitial).

We also explored coordinated hops that involve a reorientation of the interstitial Li dumbbell as illustrated in Figure 3.3.2a or 3.3.2b. The barrier for this hop mechanism, however, is substantially higher, having a value of 360meV. In fact, simply rotating the interstitial Li dumbbell between two stable orientations around the same oxygen octahedron as illustrated in Figure 3.3.2b has a barrier of 410meV for Li_3OCl (375meV for Li_3OBr). The rotational motion, therefore, occurs far less frequently

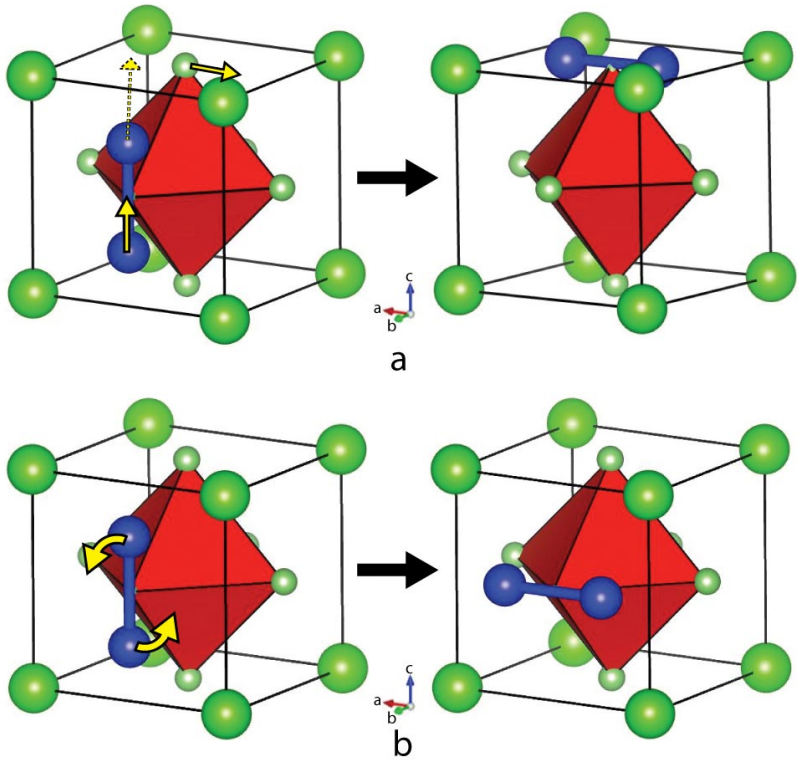

Figure 3.11: Alternative migration pathways for a dumbbell interstitial. (a) shows a perpendicular rotation to switch planes of movement, while (b) shows an in-plane rotation.

than coordinated dumbbell hops between different octahedral corner sites as illustrated in Figure 3.10. This suggests a transport mechanism consisting of extended correlated diffusion within a particular (001) plane that is occassionally reoriented through a far less likely rotation mechanism of Figure 3.3.2a or 3.3.2b.

Because of the higher conductivity seen experimentally with a mixture of Cl and Br, we also explored migration barriers in $Li_3OCl_{0.5}Br_{0.5}$. Our study of phase stability in the $Li_3OCl_{1-x}Br_x$ ($0 \leq x \leq 1$) pseudo-binary predicts a solid solution (in agreement with experiment[12]), which means that the mixed compound will exhibit disorder among Cl and Br. As a way of mimicking this disorder, we used a microstate sampled with Monte Carlo simulations at room temperature in the same 4x4x4 sized supercell to use for diffusion calculations with different local environments. We considered the low barrier interstitial-dumbbell hop mechanism illustrated in Figure 3.10. We

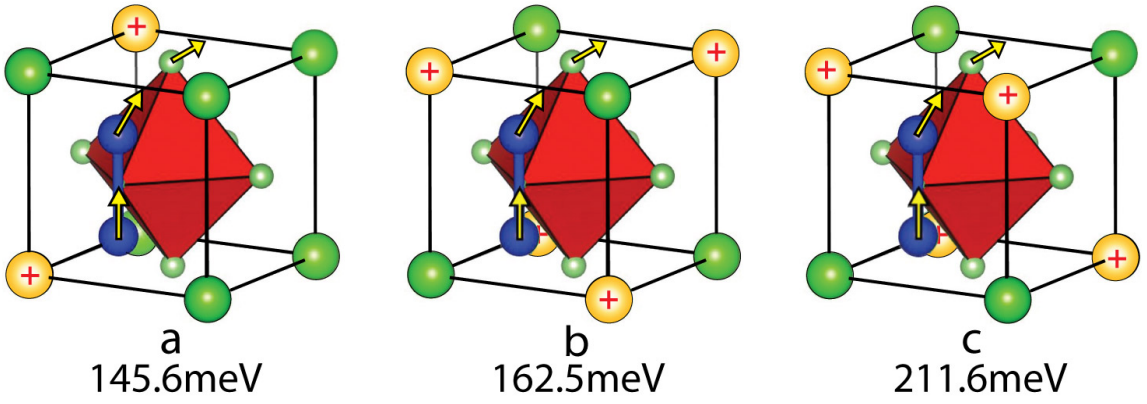

Figure 3.12: Migration barriers for local $Li_3OCl_{0.5}Br_{0.5}$ environments. Br is denoted by yellow spheres with red pluses while Cl are denoted by green spheres.

investigated hops in three different local environments in this disordered configuration. The local environments and their relation to the hop are illustrated in Figure 3.12. Calculated migration barriers for these hops had a range of energy barriers with values of 145 meV, 165 meV and 210 meV. Our calculations of migration barriers in a configuration representative of thermal disorder at 300 K as obtained with Monte Carlo simulations show that some barriers in $Li_3OCl_{0.5}Br_{0.5}$ are lower than those found in pure Li_3OCl and Li_3OBr while other barriers can be higher than in the pure compounds. There will therefore be trajectories that the interstitial dumbbells can follow with lower barriers than in the pure compounds, which is likely to result in higher conductivities in the mixed solid solution. Other compositions along $Li_3OCl_xBr_{1-x}$ can also be investigated to maximize conductivity. The limited number of local environments considered in $Li_3OCl_{0.5}Br_{0.5}$ indicates that environments with higher concentrations of the larger Cl ions correlate with lower migration barriers. A rigorous way of establishing the effect of Cl-Br disorder on the Li interstitial dumbbell mobility is to perform kinetic Monte Carlo simulations using a local cluster expansion that describes the dependence of the migration barrier on the Cl-Br configuration[48],[49],[71],[72].

3.4 Conclusions

Our first-principles study of Li_3OCl and Li_3OBr has revealed the stability of an interstitial Li dumbbell that can migrate through a collective hop mechanism with a barrier of only 175meV. This dumbbell mechanism contrasts with mechanisms in other known superionic solid electrolytes that rely on a large number of vacant crystallographic sites to facilitate lithium-ion transport. We also find that Li_3OCl (Li_3OBr) is metastable relative to decomposition into Li_2O and LiCl (Li_2O and LiBr) at oK, however, it should become stable at high temperature due to vibrational excitations. Even if decomposition into Li_2O and LiCl can be kinetically suppressed, Li_3OCl still becomes susceptible to decomposition into Li_2O_2 and LiCl, and $LiClO_4$ above approximately 2.5 V relative to a metallic lithium anode. This suggests that Li_3OCl may only be suitable for low voltage Li-batteries.

CHAPTER IV

Mg_xTiS_2 as a Cathode for Mg-ion Rechargeable Batteries

In this chapter, we explore Mg_xTiS_2 to its well-known analog, Li_xTiS_2 in order to systematically elucidate reasons for experimentally-found poor diffusion. We perform calculations within the LDA of DFT as well as GGA with van der Waal's corrections applied. Due to the accuracy of optB86 (see Figure 2.2 in Section 2.3) in predicting the c-lattice parameter of TiS2 we report results calculated with this approximation with traditional LDA and optB88 in figure comparisons. Although LDA routinely underestimates the c-lattice parameter in intercalation compounds, we find that it still serves as a reasonable predictor for properties, and all three approximations (optB86, optB88 and LDA) predict the same qualitative trends. We perform a systematic analysis of thermodynamic and kinetic properties of this system and conclude that although thermodynamically the two systems are near identical, kinetically, magnesium's extra electron prevents adequate migration from occurring.

4.1 Phase Stability

4.1.1 Global Phase Stability

We explored the relative phase stability of four layered forms of Mg_xTiS_2 as well as that of the spinel form of Mg_xTiS_2 as a function of Mg concentration. The four layered forms of Mg_xTiS_2 were characterized by different stacking sequences of the TiS_2 slabs. Each TiS_2 slab consists of an AB stacking of close-packed two-dimensional triangular lattices of sulfur. The Ti atoms occupy octahedrally-coordinated interstitial sites between the sulfur planes. As candidate layered host structures, we considered O1, O3, P3 and P2, using the nomenclature introduced by Delmas et al[73]. $LiTiS_2$ is stable in the O1 host (having an ABAB stacking sequences of close-packed sulfur layers) and maintains that host structure during deintercalation[74],[75],[48]. The O3 host (having an ABCABC stacking sequence of sulfur planes) is a common host of layered lithium-transition metal oxides such as Li_xCoO_2 and $Li_x(Ni_{1/3}Mn_{1/3}Co_{1/3})O2$ while P3 (ABBCCA) and P2 (ABBA), which have trigonal prismatic sites in the intercalation layers, are common among many Na-intercalation compounds.

We calculated the energies of 212 symmetrically distinct Mg-vacancy configurations over the octahedral sites of the O1 form of TiS_2, 300 configurations over the octahedral sites of the O3 host and 75 and 34 configurations over the prismatic sites of the P3 and P2 host structures, respectively. Similar to Li, we found that Mg prefers the octahedral sites to the tetrahedral sites in O1, O3 and the spinel form of TiS_2. We also calculated the energies of 169 Mg-vacancy configurations over the octahedral sites of the spinel form of TiS_2. We used these energies to parameterize cluster expansions of the configurational energy for each layered crystal structure and the spinel structure to determine whether any lower energy configurations exist within large supercells.

Figure 4.1 shows the calculated formation energies of all the Mg-vacancy configu-

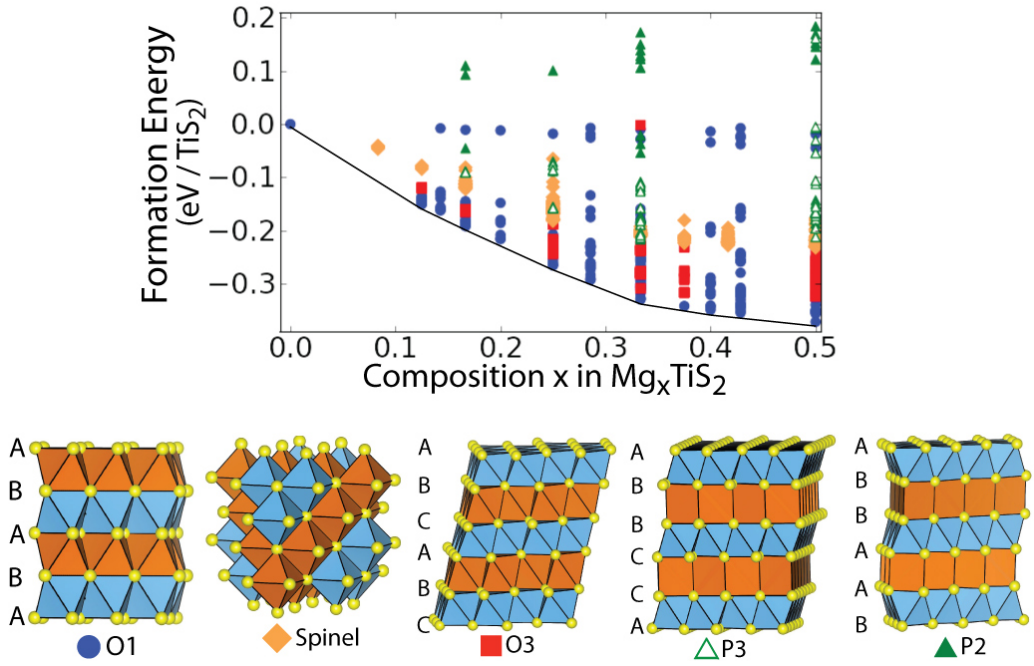

Figure 4.1: Formation energies calculated with PBE and the optB86 vdW correction for the spinel and various layered forms of Mg_xTiS_2. The O1 structure is the most stable across the entire composition range. Colors and shapes indicate different stacking sequences

rations considered within the five host structures of Mg_xTiS_2 ($0 \leq x \leq 0.5$). The O1 form of Mg_xTiS_2 has the lowest formation energy for all values of x between 0 and 0.5. The other layered host structures, while less stable than O1, on the whole have lower formation energies than the spinel form of Mg_xTiS_2.

As mentioned in Chapter 2.3, LDA regularly underpredicts lattice parameters of intercalation materials, however qualitative trends are predicted well. With this in mind, we have compared LDA to the newer van der Waals correction methods to PBE within GGA as shown in Figure 4.2. The legend is identical to that of Figure 4.1, and Figure 4.2b is the same as the hull shown in Figure 4.1. The two van der Waal's correction methods as well as LDA all predict the same qualitative trends: O1 is the lowest across all compositions, O3 is slightly higher in energy followed by spinel and the trigonal prismatic stackings.

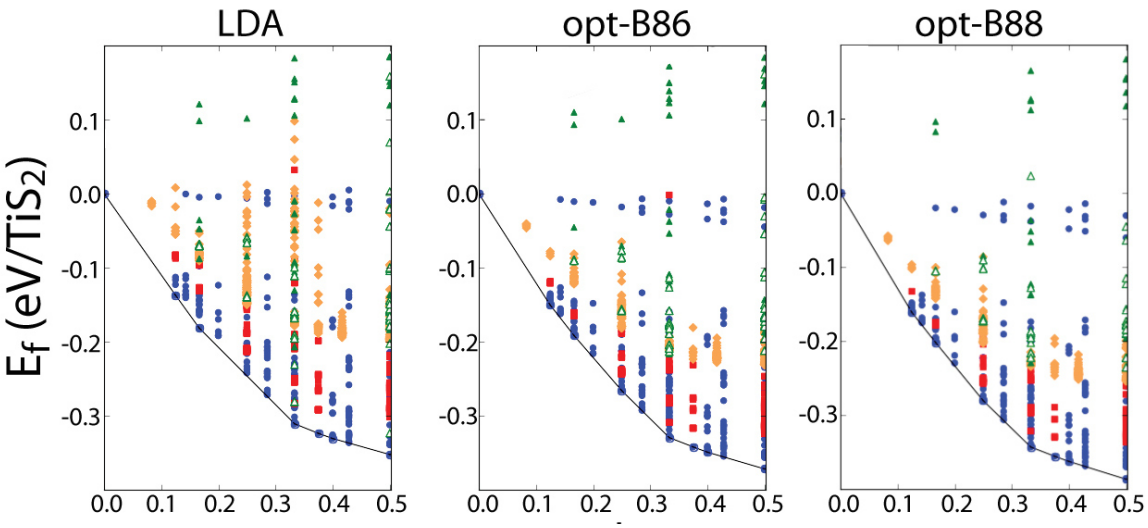

Figure 4.2: Formation energies from composition TiS_2 (x=0) to $Mg_{0.5}TiS_2$ (x=0.5) for all stacking sequences with LDA (a), opt-B86 (b), and opt-B88 (c). Qualitative trends remain the same across all three calculation schemes.

4.1.2 Phase Stability in the O1 Phase

A variety of ordered phases are predicted to be stable at intermediate Mg concentration in the O1 host structure. These ordered phases have formation energies that reside on the convex hull in Figure 4.1.

While ground states are predicted at six different concentrations, three are stable in wide Mg chemical potential ranges. The first of these stable ordered phases is $Mg_{1/6}TiS_2$ in which every other layer of Mg sites is completely empty while the remaining alternating layers are one-third filled (Figure 4.3).

This staging predicted for Mg_xTiS_2 is similar to that in graphite[76], $LiTiS_2$[77], and LiCoO2 [78],[79]. The next stable ground state is $Mg_{1/3}TiS_2$ in which every layer has one-third filling. The Mg ions order in a supercell within the filled layers of $Mg_{1/6}TiS_2$ and $Mg_{1/3}TiS_2$. This in plane ordering changes to row ordering in $Mg_{1/2}TiS_2$ as shown in Figure 4.3. Figure 4.4. In-plane ordering of the ground states shown in Figure 4.3 remains the same for LDA, optB88 and optB86. A comparison of these three formation energy hulls is shown in Figure 4.4.

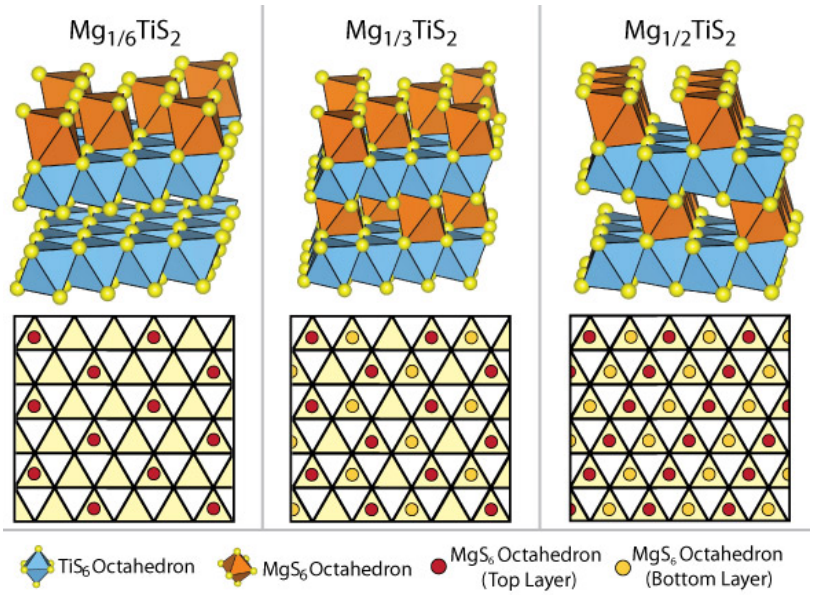

Figure 4.3: Mg in-plane ordering in the three most stable ground states of O1 Mg_xTiS_2 ($0 \leq x \leq 0.5$) along with projections of the Mg ordering within the intercalation layers. Yellow triangles denote potential octahedral Mg sites. Red circles correspond to Mg ions in one layer while yellow circles denote Mg atoms occupying the adjacent layer. Sulfur atoms occupy the vertices of each triangle. The white triangles denote tetrahedral sites

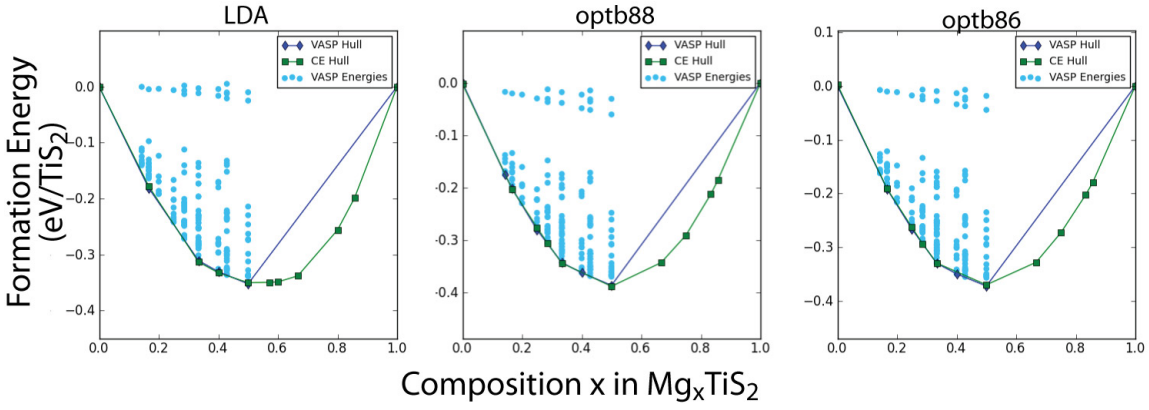

Figure 4.4: Calculated 0K hulls in the O1 phase using LDA (left), optB88 (middle), and optB86 (right). All three show the same ground state ordering. The green line with squares are the predicted cluster-expanded ground states, and the blue line with circles are the DFT ground states

4.1.3 Phase Stability in the Spinel Phase

In the spinel phase, a complete solid solution is predicted across the entire composition range Mg_xTiS_2 ($0 \leq x \leq 0.5$). This is again true across LDA, and the two vdW corrections, optB88 and optB86.

4.1.4 Voltage Predictions

Using the ground state energies, we calculated Mg chemical potentials at room temperature by applying Monte Carlo simulations to first-principles parameterized cluster expansions of the configurational energy of Mg-vacancy disorder in the O1 and spinel host structures. The cluster expansions were fit to the DFT-calculated formation energies, and grand-canonical Monte Carlo simulations were performed to calculate the dependence of the chemical potential on Mg concentration at room temperature, which was then inserted into the Nernst equation (see Chapter II) to determine the voltage profile. Figure 4.5 shows the calculated voltage profile for O1 Mg_xTiS_2 within LDA and GGA with van der Waal's corrections. The steps in the voltage profile are due to Mg-vacancy ordering at $x=\frac{1}{6}$, $\frac{1}{3}$ and $\frac{1}{2}$. LDA has more pronounced steps than the two other approximations, indicating stronger tendency to order within LDA than the approximations corrected for vdW interactions.

Contrary to the layered O1 material, spinel Mg_xTiS_2 exhibits more of a solid solution (shown in Figure 4.6, as is evident from the sloping voltage profile across the entire composition range . This behavior is similar to spinel Li_xTiS_2 [80],[81]. Electrostatic interactions between Mg (with a nominal valence of +2), are likely more screened in the three-dimensional spinel host compared to the layered two-dimensional O1 host, thereby decreasing an energetic tendency to order at intermediate concentrations.

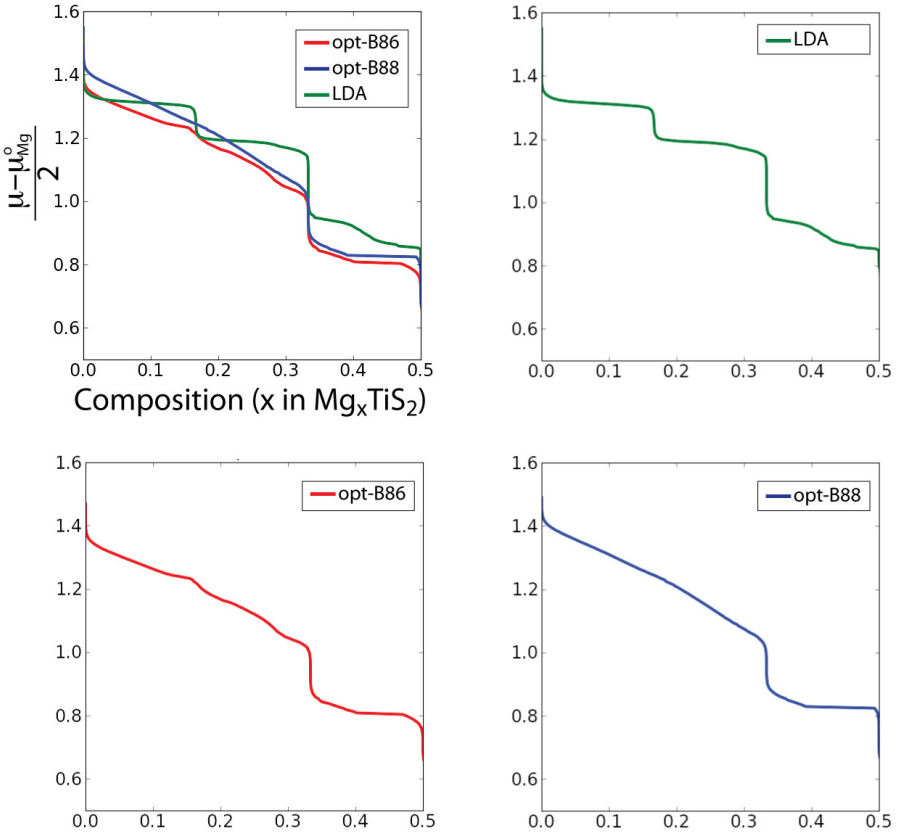

Figure 4.5: The O1 Mg_xTiS_2 voltage curve calculated with Monte Carlo simulations at 300K applied to a cluster expansion that was parameterized with PBE-optB86 (red), opt-B88 (blue), and LDA (green) energies.

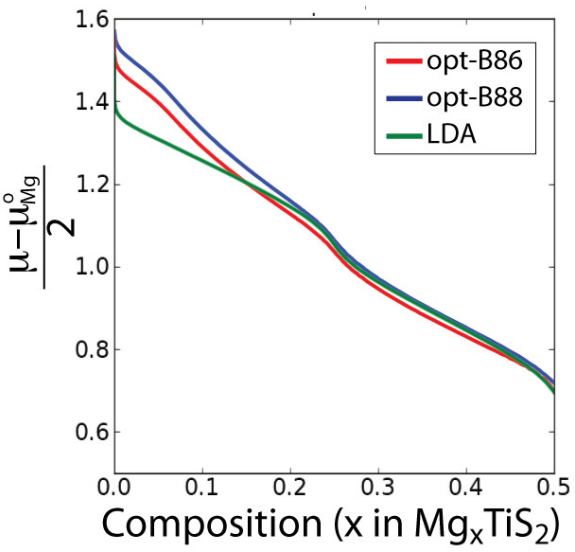

Figure 4.6: The spinel Mg_xTiS_2 voltage curve calculated with Monte Carlo simulations at 300K applied to a cluster expansion that was parameterized with PBE-optB86 (red), opt-B88 (blue), and LDA (green) energies

4.2 Diffusion

We also explored diffusion in the spinel and O1 host structures. Similarly to layered and spinel Li_xTiS_2[80],[48], layered Li_xCoO_2[82] and other layered transition metal oxides38, Mg ions in TiS2 are predicted to migrate through a neighboring tetrahedral site where the energy exhibits a local minimum before moving to the adjacent octahedral site. However, the energy barriers for Mg^{2+} diffusion are substantially greater than for Li+ diffusion.

4.2.1 Diffusion in Layered O1 Structure

Figure 4.7 shows a migration barrier at dilute Mg concentrations as calculated in a 4 x 4 x 2 supercell of the primitive O1 structure, consisting of 32 TiS_2 formula units (i.e. composition $MgTi_{32}S_{64}$). The maximum barrier of 1.16eV occurs when the Mg^{2+} passes through the face of a triangle created by three of the sulfur atoms in the MgS_6 octahedron (point β in Figure 4.7).

Because the c lattice parameter can have a large effect on migration barriers[48],[82],

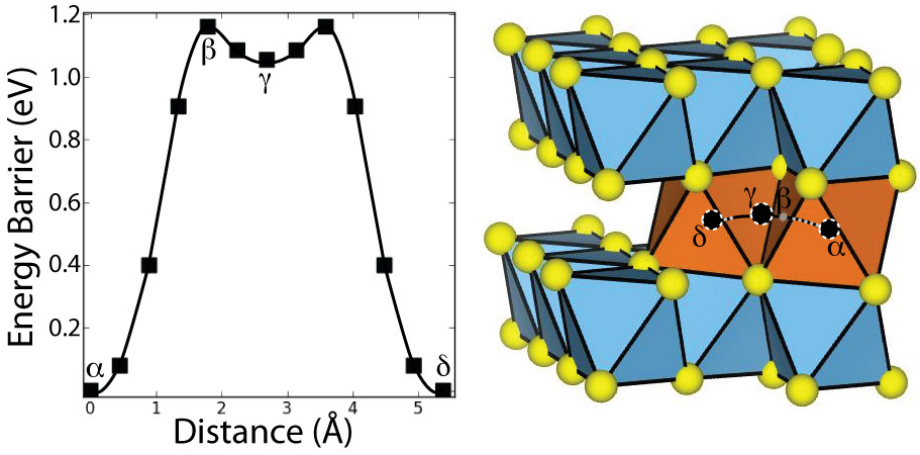

Figure 4.7: Migration pathway and barrier in dilute, O1 $MgTi_{32}S_{64}$. The pathway shows the motion of a Mg atom from an octahedral site (α) into an adjacent octahedral site (δ) through tetrahedral site which is a local minimum (γ). The maximum energy occurs when Mg passes through the trigonal face (β) shared by the octahedral and tetrahedral site.

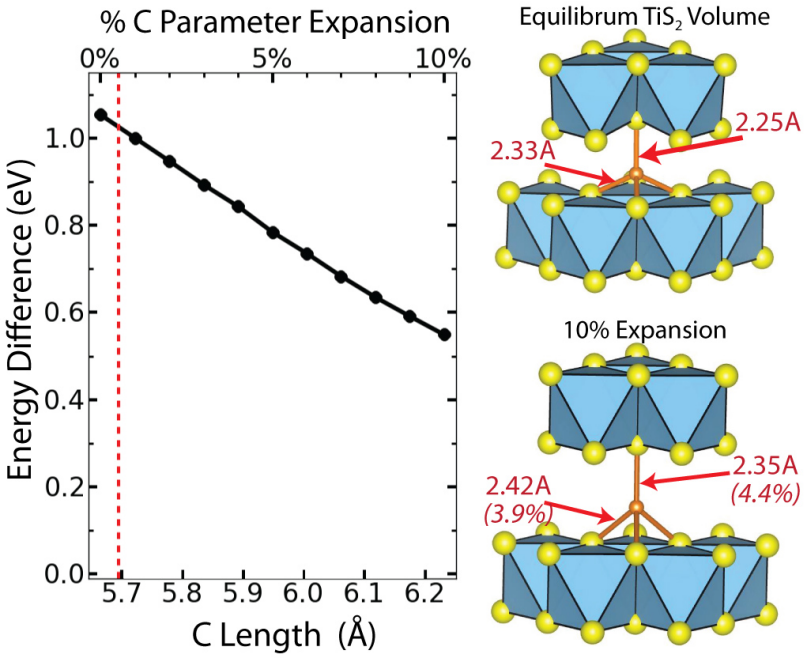

Figure 4.8: Energy differences between octahedral and tetrahedral sites in dilute O1 $MgTi_{32}S_{64}$. The dashed red line denotes the experimental c lattice parameter for TiS2 (5.7[77],[83]) and bond lengths are shown for the PBE-optB86 relaxed lattice parameters of TiS_2 and for a 10% increase of the c lattice parameter. Percentage increases are shown in italicized parentheses for the 10% expansion figure.

we examined the sensitivity of the relative stability of the tetrahedral and octahedral sites in the O1 structure as a function of dimensional changes of the host. A 4 x 4 x 2 supercell of the O1 primitive cell was created and then stretched along the c-axis. One intercalation layer (Figure 4.3) was left completely empty, while the other layer contained the magnesium atom. The Mg atom was initialized slightly off of the ideal octahedral or tetrahedral site to allow for possible relaxations to occur to a lower energy site (e.g. preferentially shifting closer to one layer of sulfurs as opposed to staying at the center). Structures were distorted along the c-axis from 1% to 10%, and then atoms were allowed to relax while the cell shape remained fixed. Figure 4.8 shows energy differences between octahedral and tetrahedral sites in the O1 layered host structure. After relaxation, the layer with the Mg ion preferentially expands, while the empty layer contracts. Figure 4.8 shows that the energy difference between tetrahedral versus octahedral occupancy decreases with increasing c-lattice parameter. This is similar to layered Li intercalation compounds[48],[82].

In addition to exploring the relative stability between tetrahedral and octahedral sites, we also investigated how a variation in the c lattice parameter affects the migration barrier between the two sites in dilute $Mg_{1/32}TiS_2$. Increasing the c lattice parameter by 5% (shown in Figure 4.9) results in a drop from 1.16eV to 0.90eV of the migration barrier. This points to a strong dependence of the migration barrier on the distance between the layers. The activated site is coordinated by three sulfur ions forming a triangle and an increase in the area of this triangle results in a lowering of the migration barrier. Further distorting the length of the c axis by 10% results in an energy barrier of 0.55eV; this is still higher than traditional Li-ion intercalation materials, indicating that artificially increasing the distances between transition metal layers does result in higher Mg mobilities, however, it is probably not low enough to achieve sufficiently high diffusion coefficients at room temperature.

As the Mg concentration increases to $Mg_{\frac{1}{3}}TiS_2$, the structure expands slightly

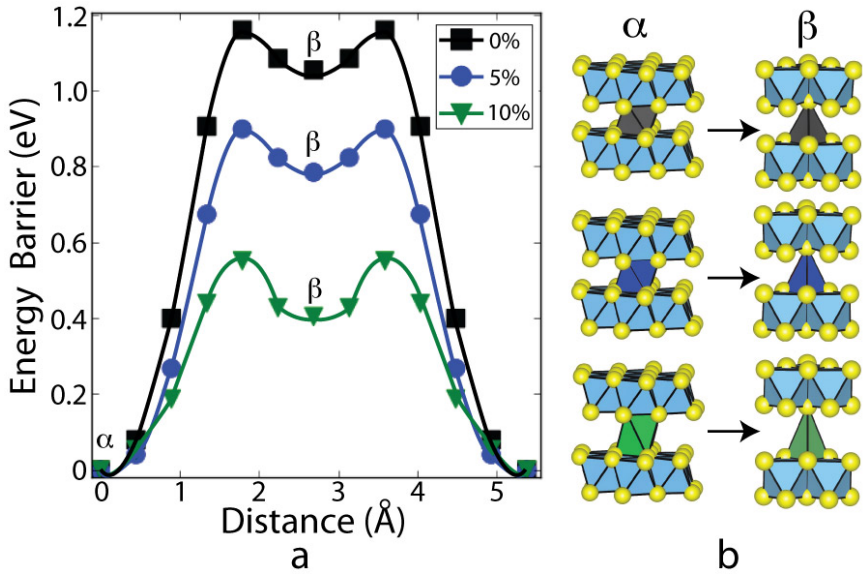

Figure 4.9: Effect of c lattice parameter increases on the migration barrier in dilute O1 $Mg_{1/32}TiS_2$. Energy barriers are shown in (a) for the equilibrium PBE+optB86 TiS_2 lattice parameters (black, top) and for a c-lattice parameter that is expanded by 5% (blue, middle) and 10% (green, bottom). Schematics of bond length increases are shown with the same color scheme in b

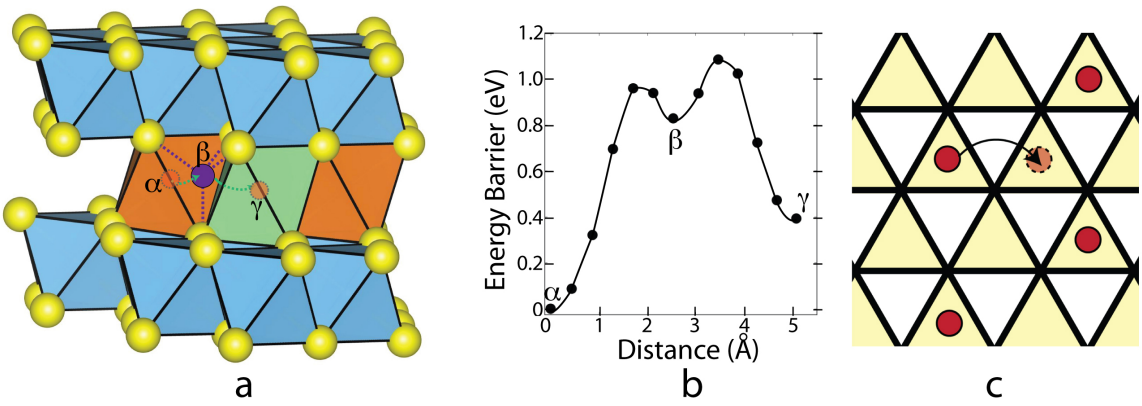

Figure 4.10: Mg hop in layered O1 $Mg_{1/3}TiS_2$. (a) Migration pathway from an octahedral site (α) to a local minimum at a tetrahedral site (purple, β) into an adjacent edge-sharing octahedron (γ, green). (b) Diffusion energy barrier and (c) Hop path as projected along the c-axis into the plane of the intercalation layer

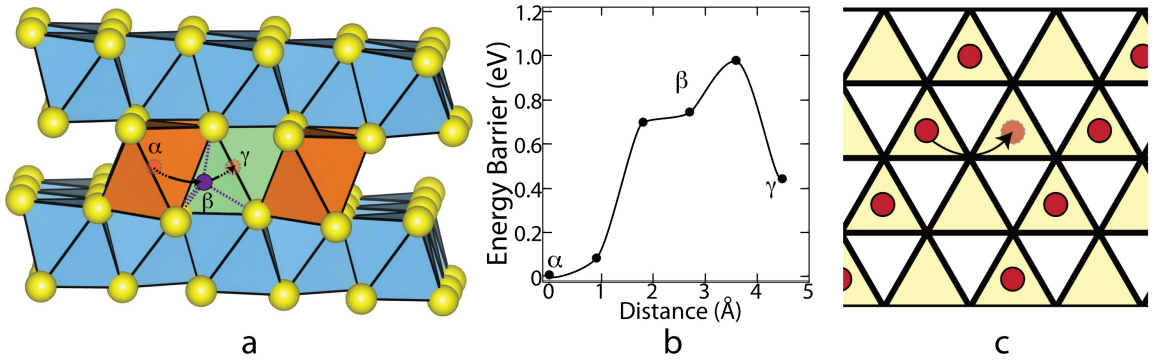

Figure 4.11: Mg hop in layered O1 $Mg_{1/2}TiS_2$. (a) Migration pathway from an octahedral site (α) to a local minimum at a tetrahedral site (purple, β) into an adjacent edge-sharing octahedron (γ, green). (b) Diffusion energy barrier and (c) Hop path as projected along the c-axis into the plane of the intercalation layer

to accommodate the extra Mg. This results in a slight decrease in the migration barrier (Figure 4.10) for a Mg ion migrating from the initial octahedral site to an intermediate tetrahedral site. However, due to the very stable $\sqrt{3}a$ x $\sqrt{3}a$ in-plane ordering in $Mg_{\frac{1}{3}}TiS_2$, any rearrangement of Mg due to diffusion will result in an increase in the energy of the end states of the hop as shown in Figure 4.10b. It is well known that self-diffusion coefficients can drop dramatically at stoichiometric compositions corresponding to stable ordered phases[82]. Often though, this drop in the self-diffusion coefficient is compensated by a rapid increase with concentration of the thermodynamic factor, minimizing the effect of ordering on the chemical diffusion coefficient appearing in Ficks first law of diffusion[82].

Similar behavior is predicted in the $Mg_{\frac{1}{2}}TiS_2$ ground state ordering as shown in Figure 4.11. A hop involving a Mg within one of the ordered rows is accompanied by an increase of the energy of the end state of the hop (Figure 4.11b), as this end state disrupts the energetically stable ordering. Nevertheless, the overall migration barrier is lower than that at more dilute Mg concentrations, in part due to an increase in the c-lattice parameter with Mg concentration.

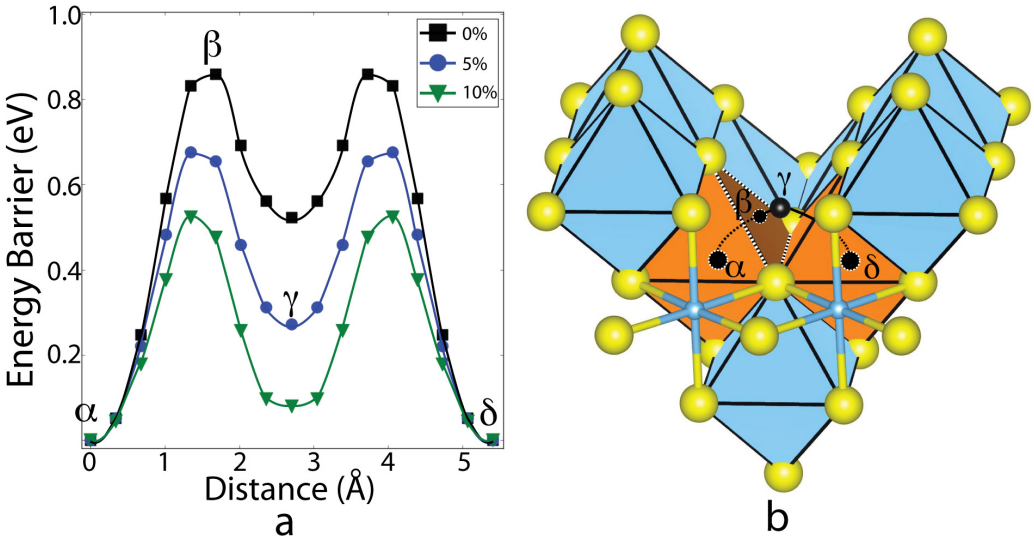

Figure 4.12: Diffusion in dilute $MgTi_{32}S_{64}$ in the spinel structure. (a) shows the diffusion barrier across path shown in (b). The black line with squares shows the barrier at equilibrium $Ti_{32}S_{64}$ lattice parameters calculated with GGA and optB86 for the van der Waal's correction. The blue line with circles shows the barrier if the volume is expanded 5%.

4.2.2 Diffusion in Spinel Structure

The Mg migration barriers in the spinel host in the dilute limit are substantially lower than in the layered form at dilute concentrations. The barrier for a Mg hop from an octahedral site to a tetrahedral site is 0.86 eV at the equilibrium spinel TiS_2 lattice parameters. These barriers were calculated in the 2 x 2 x 2 supercell of the primitive spinel crystal structure (with the composition $MgTi_{32}S_{32}$). Figure 4.12 illustrates the pathway at dilute Mg concentrations. Like the layered compound, the tetrahedral site is a local minimum. In fact, the tetrahedral site resides in a deeper energy well in the spinel host structure than in the O1 host.

We also examined the dependence of the energy differences between octahedral and tetrahedral sites on the volume of the spinel crystal structure. These calculations were performed for a single Mg in a 2 x 2 x 2 supercell of the primitive spinel crystal (with the composition $MgTi_{32}S_{32}$), incrementally increasing the volume to 10% and allowing for internal atomic relaxations at each volume. These results are shown in

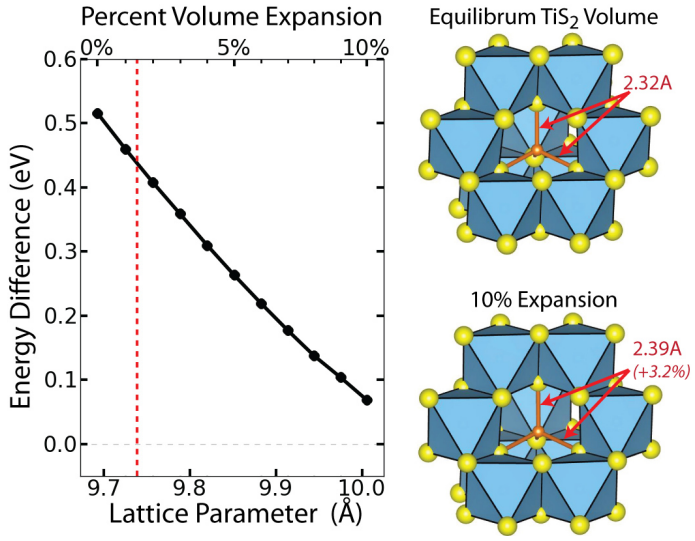

Figure 4.13: The effect of a volume increase on the difference in energy between tetrahedral versus octahedral occupancy by Mg in spinel $MgTi_{32}S_{64}$. The dashed red line shows the experimental lattice parameter at 9.737A[84] of spinel TiS_2. Bond lengths are shown for the relaxed structures for the PBE-optB86 TiS_2 parameters and for lattice parameters corresponding to a 10% increase in volume.

Figure 4.13. A nudged elastic band calculation at a 5% increase in volume predicts a decrease in the overall migration barrier by 0.2eV, to 0.68 eV, shown in Figure 4.13a. These barriers, however, are too high to ensure mobilities comparable to Li-intercalation compounds at room temperature.

4.3 Charge Distribution

The insertion of a cation into an intercalation compound results in some degree of rehybridization between the transition metals and anions of the host[85]. For example, in Li_xCoO_2, an increase in Li concentration progressively increases the ionic character of the cobalt-oxygen bonds due to a reduction in the hybridization between Co d-states and oxygen p-states as the electron from Li is donated to the host[50],[84]. Mg donates two electrons to the host and consequently induces more rehybridization between the cation and the anion than occurs with Li intercalation. In this section,

we explore the degree of rehybridization between Mg and Li insertion into both the layered and spinel crystal structures and how it may affect the migration barrier for diffusion.

In TiS_2, bonding between Ti and S has substantial covalent character. The Ti cations reside in the octahedral sites of the close-packed sulfur sublattice. The ligand field of the negatively charged sulfur anions splits the degeneracy of the Ti 3d orbitals: the $d_{3z^2-r^2}$ and $d_{x^2-y^2}$ orbitals, with lobes pointing directly towards the negatively charged sulfur anions along the Ti-S bonds, are raised in energy, while the d_{xy} , d_{yz} and d_{yz} orbitals with lobes pointing between sulfur anions are less affected. In addition to a ligand field splitting, there is also covalent hybridization between Ti and S, with σ bonds forming between sulfur p-states and Ti $d_{3z^2-r^2}$, $d_{x^2-y^2}$, 4s, and 4p states.

The degree of covalency of the σ bonds between the sulfur p-states and the Ti and orbitals changes upon insertion of Li or Mg to the TiS_2 host. The electrons accompanying Li or Mg upon insertion into the TiS_2 are donated to the host and fill the lower non-bonding Ti d_{xy} , d_{yz} and d_{yz} orbitals that point between the sulfur anions. The increased negative charge around the Ti ions in turn raises the energy of the d-states relative to the sulfur p-states, causing a reduction in the covalency and an increase in polarization of the σ bond made of the Ti and $d_{3z^2-r^2}$ and $d_{x^2-y^2}$ orbitals and the sulfur p-orbitals. The shift from covalent bonding to more ionic bonding between Ti and S increases the charge around the sulfur anions. The sulfur anions most affected are those directly coordinating the inserted Mg or Li cation, whose effective positive valence polarizes the negative charge towards it.

Figure 4.14 shows charge difference plots as Mg (Li) is inserted in an octahedral site and a tetrahedral site of the O1 form of TiS_2. These charge difference plots were obtained by subtracting the charge density of TiS_2 from the charge density of Mg_xTiS_2 and Li_xTiS_2 for crystal structures in which Ti and S are at identical positions. The

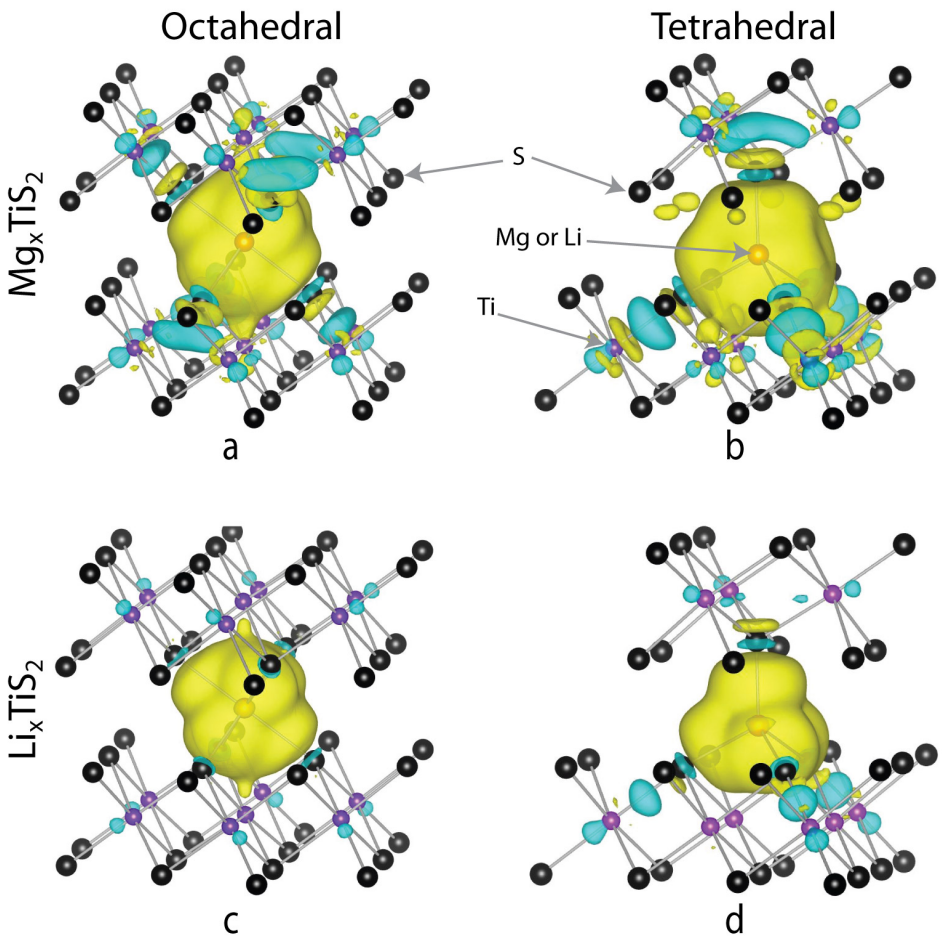

Figure 4.14: Charge difference plots of layered TiS_2 having the O1 crystal structure with an isolated Mg (x=$\frac{1}{32}$ in (a) an octahedral site and (b) a tetrahedral site and with an isolated Li (x=$\frac{1}{32}$) (c) in an octahedral site and (b) in a tetrahedral site. Blue regions denote areas of charge depletion while yellow regions denote charge accumulation. The intercalating species sits at the center of the yellow cloud of charge accumulation and is coordinated by sulfur atoms (black) and further out sit Ti atoms (purple). Ti-S bonds are drawn to better show d orbital rehybridization

charge density plots therefore show where the valence electrons accompanying Mg and Li reside in the host and how they modify the original charge density of TiS_2. Yellow signifies an accumulation while blue signifies a depletion of electron density. As is clear for both Mg and Li insertion, there is substantial charge polarization towards the inserted cation. The polarization is more pronounced around Mg compared to Li, as is to be expected considering the higher positive valence of Mg. The rehybridization of the Ti d-orbitals is also clearly evident. The d-orbitals pointing along the Ti-S bond ($d_{3z^2-r^2}$ and $d_{x^2-y^2}$) towards the sulfur coordinating the inserted Mg or Li undergo a depletion of electron density, resulting in less overlap between Ti-d orbitals and S-p orbitals. Simultaneously, non-bonding d-orbitals (i.e. a combination of d_{xy}, d_{xz} and d_{yz}) that point between S ions accumulate charge density. As is clear in Figure 4.14, the rehybdridization around Ti upon Mg insertion is substantially larger than that associated with Li insertion due to the introduction to the host structure of two electrons per Mg as opposed to one for Li.

As an Mg or Li ion migrates through the crystal, it will drag its electron cloud residing on the coordinating sulfur anions with it. The surrounding Ti and sulfur cations will therefore be required to rehybridize as the cation moves. Figure 4.14 shows that the rehybridization around Ti is stronger when Mg or Li resides in the tetrahedral site compared to the octahedral site. The lower S coordination of the tetrahedral site compared to the octahedral site concentrates rehybridization over fewer bonds, thereby making it more pronounced for the tetrahedral site.

Figure 4.15 compares charge difference plots for Mg insertion into tetrahedral sites of O1 and spinel TiS2. While the O1 and spinel hosts both consist of close packed anion sublattices, the different arrangements of the Ti ions over the octahedral sites result in differing degrees of rehybridization. The charge difference plots of Figure 4.15 were calculated using identical Ti-S and S-S nearest neighbor bond lengths in ideal, unrelaxed structures to remove any effects that atomic relaxations have on charge

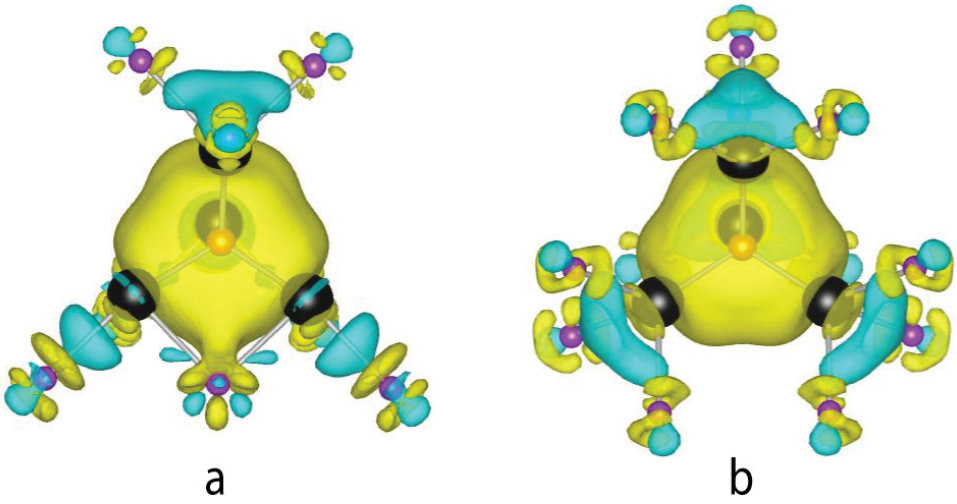

Figure 4.15: Charge difference plots of layered TiS_2 in either the O1 or spinel crystal structure with an isolated Mg (x=$\frac{1}{32}$ in a tetrahedral site. Blue regions denote areas of charge depletion while yellow regions denote charge accumulation. All S-S bonds are identical for both spinel and O1 to isolate effects the Ti environment has on charge rehybridization. All atoms not undergoing charge re-hybridization have been hidden for clarity. The spinel structure has 12 Ti atoms participating in charge re-hybridization located in four groups of three Ti atoms, while the O1 structure has 9 Ti atoms participating in charge rehybridization, with one group of three shown at the top of (a) and the remaining six clustered in a network at the bottom of (a).

distribution. As is clear in Figure 4.15, the rehybridization in the spinel tetrahedral sites is more evenly distributed than in the tetrahedral site of layered O1. In spinel, each S anion coordinating a tetrahedral Mg or Li site hybridizes with three Ti. In layered O1, only one of the four S anions coordinating a tetrahedral site hybridizes evenly with three Ti (the top sulfur atom in Figure 4.15a), while the remaining three S hybridize primarily with only one Ti each and partially hybridize with two additional Ti that are shared by the other S anions. The rehybridization per Ti-S bond upon Mg insertion into a tetrahedral site is therefore more pronounced in the layered host than in spinel.

4.4 Discussion

In this chapter, we have studied the thermodynamic, kinetic and electronic properties of $MgTiS_2$ in common intercalation compound crystal structures. Thermodynamically, Mg_xTiS_2 and Li_xTiS_2 are stable in similar structures. For both, the spinel structure is metastable, and the layered O1 compound is energetically preferred at all compositions. Mg and Li also prefer the octahedral sites to the tetrahedral sites in both forms of TiS_2. The voltage profiles for both Li and Mg insertion into the two TiS_2 hosts are also qualitatively similar, although Mg intercalation results in more stable intermediate ordered phases than Li intercalation, as manifested by steps in the voltage profile[48],[80]. The increased stability of Mg-vacancy ordering at room temperature as compared to similar Li-vacancy ordering within TiS_2 is likely due to larger electrostatic interactions between Mg^{2+} ions. The mobilities of Mg and Li in both O1 and spinel TiS_2 differ substantially. Although Li and Mg are predicted to hop with the same mechanism, passing through an intermediate tetrahedral site, the Mg mobility within the TiS_2 host structures is significantly lower than that of Li due to much larger migration barriers (Figures 5,7-10). The Mg diffusion coefficients in TiS_2 will therefore have quantitative values that are more typical of substitutional

diffusion43 in alloys than that of interstitial diffusion[48],[82],[80],[86],[87]. As with Li diffusion, the migration barrier for Mg diffusion is very sensitive to the lattice parameter c of the O1 host and to the volume of the spinel host[48],[82],[86],[88],

The migration barriers for both Li and Mg hops between octahedral sites in layered O1 and spinel TiS_2 correlate with the difference in energy between octahedral site and tetrahedral site occupancy. Several factors that contribute to the difference in site energies between tetrahedral and octahedral sites can be identified. One is the size of the site and the flexibility of coordinating ions of the particular host crystal structure to relax once occupied by an intercalating species. Another is the electrostatic energy, which may be more favorable in one interstitial site relative to the other. There are also more complex quantum mechanical effects including the flexibility of adjacent ions to rehybridize as the positively charged cation migrates from one site to another.

The DFT calculations reported on here predict that the migration barriers for Mg diffusion in the dilute limit are lower in spinel than in O1 TiS_2. A lower barrier in spinel compared to O1 suggests that electronic factors play an important role since the sulfur anions forming the tetrahedral sites of layered intercalation compounds have more degrees of freedom to relax than those in the spinel host due to fewer symmetry constraints imposed by the layered crystal structure. Furthermore, the tetrahedral site of O1 does not share a face with a transition metal cation, as occurs in layered O3, a crystal structure adopted by many transition metal oxide intercalation compounds. A cation in the O1 host therefore does not experience the strong electrostatic repulsions with face-sharing transition metal cations that increases the tetrahedral site energy relative to that of the octahedral site.

There are no unambiguous ways to disentangle the role of purely electrostatic interactions from the quantum mechanical interactions responsible for rehybridization. Nevertheless, the charge difference plots comparing charge redistribution upon Mg insertion into tetrahedral sites (Figure 4.15) show that the degree of rehybridization

per Ti-S bond is more pronounced in O1 than in spinel TiS_2. This is due to the higher coordination of the tetrahedral S anions by Ti in the spinel host compared to the layered O1 host. As shown in Figure 4.15, the rehybridization is concentrated over fewer Ti-S bonds (9) in O1 than in spinel (12).

While enlarging the size of the interstitial network of the intercalation compound can clearly play a role in reducing the migration barrier for Mg diffusion (evident from examining the tetrahedral and octahedral site energy differences at increasing volumes or c-lattice parameter), electronic factors are also important. Based on the predicted differences in migration barriers between spinel and O1, lower migration barriers may be achievable using transition metal ions that are more flexible at rehybridizing. In this sense, those transition metal cations that are capable of shifting more than one valence state are likely to be more flexible in rehybridizing as the cation migrates through the crystal. The lower migration barrier in spinel compared to O1 also suggests that a higher coordination of the anion sublattice with transition metal cations is likely to reduce the migration barrier as it distributes the rehybridization over more metal-anion bonds. These features are present in the Mo_6X_8 (X=S, Se) Chevrel phases exhibiting reasonable Mg mobilities, where the transition metal to anion ratio is higher than in most intercalation compounds and where Mo has the flexibility to shift two valence states.

4.5 Conclusions

Using first principles and statistical mechanics tools, we systematically investigated $MgTiS_2$ and compared it to its well-studied Li counterpart, $LiTiS_2$. We find that Mg in both the layered and spinel forms of TiS_2 occupy the same sites as Li ions in Li_xTiS_2 (i.e. the octahedrally coordinated interstitial sites). Furthermore, Mg intercalation into the layered form of TiS_2 does not induce changes in the stacking sequence of the TiS_2 slabs. Predicted voltage profiles are similar to those of $LiTiS_2$,

but show pronounced steps due to strong thermodynamic tendencies for Mg-vacancy ordering over the octahedral sites. We also find that the Mg diffusion mechanisms are identical to those of Li in layered and spinel TiS_2, whereby the migration between neighboring octahedral sites involves the passage through an intermediate tetrahedral site. Nevertheless, contrary to Li diffusion in $LiTiS_2$[80],[48], Mg mobility is very sluggish at room temperature, with typical migration barriers predicted to be of the order of 1eV. Considering that the sulfides exhibit among the most facile Li insertion and removal kinetics of all layered intercalation compounds (including the oxides), this result suggests that popular intercalation host chemistries and crystal structures for Li-ion batteries are unlikely to be suited for Mg intercalation at room temperature. An analysis of the dependence of Mg migration barriers on dimensional changes of the host, however, indicates that the size of the migration channel between adjacent sites is an important factor in determining migration barriers. Electronic effects are also likely to play an important role since the rehybridization between transition metal and anion is more severe upon Mg insertion than upon Li insertion. Transition metals that are more flexible in shifting valence and that thereby can more easily rehybridize as Mg migrates through the crystal should help to reduce migration barriers. Similarly, a higher density of transition metal-anion bonds should also help to lower migration barriers as this will reduce the degree of rehybridization per bond.

CHAPTER V

Na_xCoO_2 as a Cathode for Na-ion Rechargeable Batteries

Although the development of sodium-ion batteries began alongside that of Mg- and Li-ion batteries in the 1970's and 1980's [75],[89],[90],[91],[92], similar to that of Mg-ion research, Na-ion research dropped off in favor of Li-ion systems. However, recent years have seen a resurgence[93],[94],[95] in studying Na-ion systems primarily because of its cost advantages to that of Li-ion, however, the larger ionic radius of Na (1.06Åto lithium's 0.76Å) presents the ability to find novel intercalation structures which are unsuitable for use in Li-ion systems. With the larger ionic radius in mind, we investigate sodium intercalation into the spinel host CoO_2; lithium energetically prefers to occupy tetrahedral sites below and at the composition $Li_0.5CoO_2$ (where all possible tetrahedral sites are filled). Sodium's larger size might prevent tetrahedral sites from ever being stable, which could lead to better cycling properties than its lithium counterpart.

5.1 Phase Stability

We investigated phase stability over octahedral and tetrahedral sites over the composition range Na_xCoO_2 with $0 \leq x \leq 1$. Interestingly, we find that sodium is not

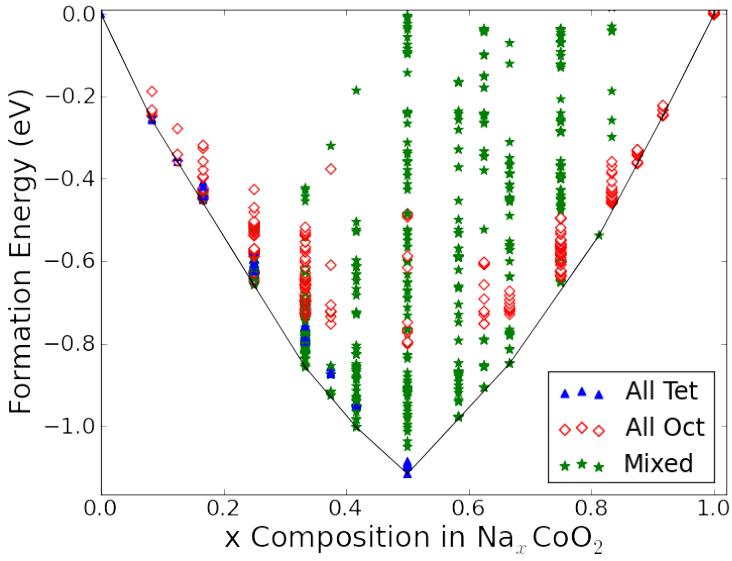

Figure 5.1: Formation energies for calculated structures along composition Na_xCoO_2 with $0 \leq x \leq 1$. Blue triangles denote structures where the sodium ions all relaxed into tetrahedral sites, open red diamonds denote structures where the sodium ions all relaxed into octahedral sites, and green stars show structures where sodium ions fill both octahedral and tetrahedral sites.

too large to avoid tetrahedral sites entirely, but instead, there is minimal preference at intermediate compositions for either tetrahedral or octahedral sites.

The lack of any obvious Na-vacancy orderings asides from those at $Na_{0.5}CoO_2$ and $NaCoO_2$ imply a solid solution over the other portions of the composition range, which is indicated by a gradual sloping of the voltage curve with steps at x=$\frac{1}{2}$ and x=1 (where all tetrahedral and all octahedral sites are filled, respectively). At compositions below $Na_{0.2}CoO_2$, tetrahedral sites are preferentially filled; at compositions (x) within $Na_{0.2}CoO_2$ <x <$Na_{0.2}CoO_2$, as well as $Na_{0.5}CoO_2$ <x <$Na_{0.8}CoO_2$, a combination of octahedral and tetrahedral sites are the lowest energy structures; at compositions x>$Na_{0.8}CoO_2$, only octahedral sites prefer to be filled.

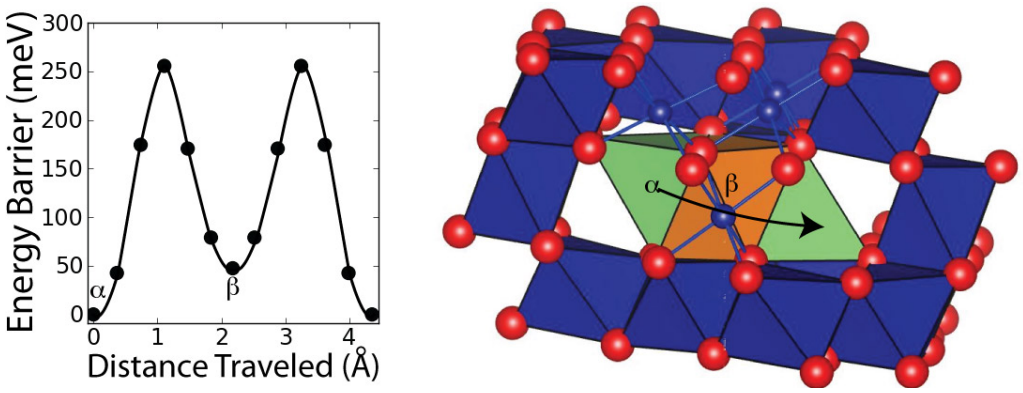

Figure 5.2: Diffusion pathway for dilute $NaCo_{32}O_{64}$ from a tetrahedral site (α) to another tetrahedral site through an octahedral site (β)

5.2 Diffusion Mechanisms

Since a mixture of octahedral and tetrahedral sites are preferred over entirely one site, energy differences between the two sites are most likely minimal, which could result in low migration barriers. We began by examining diffusion in a dilute 2x2x2 supercell of the primitive spinel structure along the path shown in Figure 5.2. We added one Na into the $Co_{32}O_{64}$ host structure. The energy differences between the octahedral and tetrahedral sites in this dilute limit is only 50meV, however, diffusing through the activated site which is the triangular face shared by the tetrahedral and octahedral site is harder, yet still good compared to its Li-ion counterparts.

Additionally, we examined diffusion in a 2x2x2 supercell of the primitive spinel structure at the composition $Na_{0.5}CoO_2$, where all tetrahedral sites are filled. When one vacancy is created, it is actually energetically favorable for the sodium atom to move from the tetrahedral site into the octahedral site. The energy difference between the octahedral and tetrahedral sites, similar to the dilute case, is only 100meV.

CHAPTER VI

Conclusions & Outlook

Moving beyond the traditional transition metal oxide cathode/liquid lithium electrolyte/graphite anode lithium-ion battery has been thus far an exciting endeavor, and it is apparent that both subtle changes (replacing Li with Na with a slightly larger ionic radius) or drastic changes (replacing a liquid electrolyte with a solid) require a great deal of investigation. First principles can help elucidate some of the problems and successes of these new materials. We have helped explain why materials which work remarkably well for Li-ion batteries will not work in their Mg counterparts (even with very similar ionic radii) through our investigation into Mg_xTiS_2. Hopefully, this points scientists to investigate completely different structures in the hopes of harnessing the benefits of Mg-ion batteries. Additionally, we discovered the mechanism for superionic diffusion in Li_3OCl,which has a structure very unlike that of other known solid electrolytes. This provides a new class of materials which could operate on defect-based diffusion as opposed to structures with a large number of open sites available for Li migration.

BIBLIOGRAPHY

BIBLIOGRAPHY

[1] J. Vetter. Ageing mechanisms in lithium-ion batteries. *Journal of Power Sources*, 147, 2005.

[2] S. P. Ong, Y. Mo, W. D. Richards, L. Miara, H. S. Lee, and G. Ceder. Phase stability, electrochemical stability and ionic conductivity of the Li 101 MP 2 X 12 (M= Ge, Si, Sn, Al or P, and X= O, S or Se) family of superionic conductors. *Energy and Environmental Science*, 6, 2012.

[3] T. Lapp. Ionic conductivity of pure and doped Li3N. *Solid State Ionics*, 11, 1983.

[4] X. Yu. A Stable Thin-Film Lithium Electrolyte: Lithium Phosphorus Oxynitride. *Journal of The Electrochemical Society*, 144, 1997.

[5] R. Kanno and M. Murayama. Lithium ionic conductor thio-LISICON: the Li2S-GeS2-P2S5 system. *Journal of The Electrochemical Society*, 148, 2001.

[6] F. Mizuno, A. Hayashi, K. Tadanaga, and M. Tatsumisago. New, highly ion-conductive crystals precipitated from Li2S-P2S5 glasses. *Advanced Materials*, 17, 2005.

[7] N. Kamaya, K. Homma, Y. Yamakawa, M. Hirayama, R. Kanno, M. Yonemura, Y. Kamiyama, T.and Kato, S. Hama, K. Kawamoto, and A Mitsui. A lithium superionic conductor. *journal*, 10, 2011.

[8] Y. Mo, S. P. Ong, and G. Ceder. First Principles Study of the Li10GeP2S12 Lithium Super Ionic Conductor Material. *Chemistry of Materials*, 24, 2005.

[9] D. Qian, B. Xu, H.-M. Cho, T. Hatsukade, K. J. Carroll, and Y. S Meng. Lithium Lanthanum Titanium Oxides: A Fast Ionic Conductive Coating for Lithium-Ion Battery Cathodes. *Chemistry of Materials*, 24, 2012.

[10] M. Xu, J. Ding, and E. Ma. One-dimensional stringlike cooperative migration of lithium ions in an ultrafast ionic conductor. *Applied Physics Letters*, 101, 2012.

[11] Y. Zhang, Y. Zhao, and C. Chen. Ab initio study of the stabilities of and mechanism of superionic transport in lithium-rich antiperovskites. *Physical Review B*, 87, 2013.

[12] Y. Zhao and L. L. Daemen. Superionic Conductivity in Lithium-Rich Anti-Perovskites. *Journal of the American Chemical Society*, 134, 2012.

[13] S. Narayanan, F. Ramezanipour, and V. Thangadurai. Enhancing Li Ion Conductivity of Garnet-Type Li5La3Nb2O12 by Y- and Li-Codoping: Synthesis, Structure, Chemical Stability, and Transport Properties. *The Journal of Physical Chemistry C*, 116, 2012.

[14] Y. Guo, J. Yang, Y. NuLi, and J. Wang. Study of electronic effect of Grignard reagents on their electrochemical behavior. *Electrochemistry Communications*, 12, 2010.

[15] M. Matsui. Study on electrochemically deposited Mg metal. *Journal of Power Sources*, 196, 2011.

[16] P.G. Bruce, F. Krok, J. Nowinski, V.C. Gibson, and K. Tavakkoli. Chemical intercalation of magnesium into solid hosts. *Journal of Materials Chemistry*, 1, 1991.

[17] J.P. Pereira-Ramos, R. Messina, and J. Perichon. Electrochemical formation of a magnesium vanadium bronze MgxV2O5 in sulfone-based electrolytes at 150C. *Journal of Electroanalytical Chemistry and Interfacial Electrochemistry*, 218, 1987.

[18] Petr Novk, Werner Scheifele, and Otto Haas. Magnesium insertion batteries an alternative to lithium? *Journal of Power Sources*, 54, 1995.

[19] P Saha, M.K. Datta, O.I. Velikokhatnyi, A. Manivannan, D. Alman, and P.N. Kumta. Rechargeable magnesium battery: Current status and key challenges for the future. *Progress in Materials Science*, 66, 2014.

[20] H.D. Yoo, I. Shterenberg, Y. Gofer, G. Gershinsky, N. Pour, and D. Aurbach. Mg rechargeable batteries: an on-going challenge. *Energy & Environmental Science*, 6, 2013.

[21] Z.-L. Tao, L.-N. Xu, X.-L. Gou, J. Chen, and H.-T Yuan. TiS2 nanotubes as the cathode materials of Mg-ion batteries. *Chemical communications*, 2004.

[22] P. Novk, R. Imhof, and O. Haas. Magnesium insertion electrodes for rechargeable nonaqueous batteries a competitive alternative to lithium? *Electrochimica Acta*, 45, 1999.

[23] P Novk. Electrochemical Insertion of Magnesium in Metal Oxides and Sulfides from Aprotic Electrolytes. *Journal of The Electrochemical Society*, 140, 1993.

[24] T. Ichitsubo, T. Adachi, S. Yagi, and T. Doi. Potential positive electrodes for high-voltage magnesium-ion batteries. *Journal of Materials Chemistry*, 21, 2011.

[25] C. Ling, D. Banerjee, W. Song, M. Zhang, and M. Matsui. First-principles study of the magnesiation of olivines: redox reaction mechanism, electrochemical and thermodynamic properties. *Journal of Materials Chemistry*, 22, 2012.

[26] C. Ling and F. Mizuno. Phase Stability of Post-spinel Compound AMn 2 O 4 (A = Li, Na, or Mg) and Its Application as a Rechargeable Battery Cathode. *Chemistry of Materials*, 25, 2013.

[27] E. Levi, G. Gershinsky, D. Aurbach, O. Isnard, and G. Ceder. New Insight on the Unusually High Ionic Mobility in Chevrel Phases. *Chemistry of Materials*, 21, 2009.

[28] E. Levi, M. D. Levi, O. Chasid, and D. Aurbach. A review on the problems of the solid state ions diffusion in cathodes for rechargeable Mg batteries. *Journal of Electroceramics*, 22, 2007.

[29] J. M. Sanchez, F. Ducastelle, and D. Gratias. Generalized cluster description of multicomponent systems. *Physica A: Statistical Mechanics and its Applications*, 128, 1984.

[30] N.W. Ashcroft and N.D. Mermin. *Solid State Physics*. Saunders College, Philadelphia, 1976.

[31] R. G. Parr and W. Yang. *Density Functional Theory of Atoms and Molecules*. Oxford University Press, 1989.

[32] O. Madelung. *Introduction to Solid State Theory*. Springer Verlag, 1978.

[33] R.O Jones and O. Gunnarsson. The density functional formalism, its applications and prospects. *Reviews of Modern Physics*, 61, 1989.

[34] P. Hohenberg and W. Kohn. Inhomogeneous Electron Gas. *Physical Review*, 136, 1964.

[35] M. Levy. Universal variational functionals of electron densities, first-order density matrices, and natural spin-orbitals and solution of the v-representability problem. *Proceedings of the National Academy of Sciences*, 76, 1979.

[36] W. Kohn and L. J. Sham. Self-Consistent Equations Including Exchange and Correlation Effects. *Physical Review*, 140, 1965.

[37] J. P. Perdew, K. Burke, and M. Ernzerhof. Generalized Gradient Approximation Made Simple. *Physical Review Letters*, 77, 1996.

[38] S. Grimme, J. Antony, S. Ehrlich, and S. Krieg. A consistent and accurate ab initio parametrization of density functional dispersion correction (dft-d) for the 94 elements H-Pu. *Journal of Chemical Physics*, 132, 2010.

[39] S. Grimme, S. Ehrlich, and L. Goerigk. Effect of the damping function in dispersion corrected density functional theory. *Journal of Computational Chemistry*, 32, 2011.

[40] S. Grimme. Semiempirical gga-type density functional constructed with a long-range dispersion correction. *Journal of Computational Chemistry*, 27, 2006.

[41] M. Dion, H. Rydberg, E. Schrder, D. C. Langreth, and B. I. Lundqvist. Van der Waals Density Functional for General Geometries. *Physical Review Letters*, 92, 2004.

[42] G. Romn-Prez and J. M. Soler. Efficient Implementation of a van der Waals Density Functional: Application to Double-Wall Carbon Nanotubes. *Physical Review Letters*, 103, 2009.

[43] J. Klimes, D. R. Bowler, and A. Michaelides. Chemical accuracy for the van der Waals density functional. *Journal of Physics: Condensed Matter*, 22, 2010.

[44] K. Lee, E. D. Murray, L. Kong, B. I. Lundqvist, and D. C. Langreth. Higher-accuracy van der Waals density functional. *Physical Review B*, 82, 2010.

[45] J Klimes, D. R. Bowler, and A Michaelides. Van der Waals density functionals applied to solids. *Physical Review B*, 83, 2011.

[46] H. Peelaers and C. G. Van de Walle. First-principles study of van der Waals interactions in MoS2 and MoO3. *Journal of Physics: Condensed Matter*, 26, 2014.

[47] J. Carrasco. Role of van der Waals Forces in Thermodynamics and Kinetics of Layered Transition Metal Oxide Electrodes: Alkali and Alkaline-Earth Ion Insertion into V2O5. *The Journal of Physical Chemistry C*, 118, 2014.

[48] A. Van der Ven, J. Thomas, Q. Xu, B. Swoboda, and D. Morgan. Nondilute diffusion from first principles: Li diffusion in LixTiS2. *Physical Review B*, 78, 2008.

[49] A. Van der Ven, G. Ceder, M. Asta, and P. Tepesch. First-principles theory of ionic diffusion with nondilute carriers. *Physical Review B*, 64, 2001.

[50] A. Van der Ven, M. K. Aydinol, G. Ceder, G. Kresse, and J. Hafner. First-principles investigation of phase stability in Li x CoO 2. *Physical Review B*, 58, 1998.

[51] V. L. Chevrier, S. P. Ong, R. Armiento, M. K. Y. Chan, and G. Ceder. Hybrid density functional calculations of redox potentials and formation energies of transition metal compounds. *Physical Review B*, 82, 2010.

[52] A. D. Becke. Density?functional thermochemistry. III. The role of exact exchange. *Journal of Chemical Physics*, 98, 1993.

[53] A. D. Becke. A new mixing of HartreeFock and local density?functional theories. *Journal of Chemical Physics*, 98, 1993.

[54] J. Heyd, G. E. Scuseria, and M. Ernzerhof. Hybrid functionals based on a screened Coulomb potential. *Journal of Chemical Physics*, 118, 2003.

[55] C. Adamo and V. Barone. Toward reliable density functional methods without adjustable parameters: The PBE0 model. *Journal of Chemical Physics*, 110, 1999.

[56] J. Paier, M. Marsman, K. Hummer, G. Kresse, I. C. Gerber, and J. G. Angyan. Screened hybrid density functionals applied to solids. *Journal of Chemical Physics*, 125, 2006.

[57] L. Wang, T. Maxisch, and G. Ceder. Oxidation energies of transition metal oxides within the GGA+ U framework. *Physical Review B*, 73, 2006.

[58] W. Bucheli, T. Durn, R. Jimenez, J. Sanz, and A. Varez. On the Influence of the Vacancy Distribution on the Structure and Ionic Conductivity of A-Site-Deficient LixSrxLa2/3-xTiO3 Perovskites. *Inorganic Chemistry*, 51, 2012.

[59] S. Hull. Superionics: crystal structures and conduction processes. *Reports on Progress in Physics*, 67, 2004.

[60] S. Hull, D. A. Keen, P. A. Madden, and M. Wilson. Ionic diffusion within the alpha and beta phases of Ag3SI. *Journal of Physics. Condensed Matter*, 19, 2007.

[61] Y. Yamane, K. Yamada, and K. Inouee. Mechanochemical synthesis and order-disorder phase transition in fluoride ion conductor RbPbF3. *Solid State Ionics*, 179, 2008.

[62] G. W. Watson, S. C. Parker, and A. Wall. Molecular dynamics simulation of fluoride-perovskites. *Journal of Physics: Condensed Matter*, 4, 1992.

[63] V. M. Bouznik, Y. N. Moskvich, and V. N. Voronov. Nuclear magnetic resonance study of fluorine-19 motion in cesium lead trifluoride. *Chemical Physics Letters*, 37, 1976.

[64] O. Reckeweg, B. Blaschkowski, and T. Schleid. Li5OCl3 and Li3OCl: Two Remarkably Different Lithium Oxide Chlorides. *Zeitschrift fr anorganische und allgemeine Chemie*, 638, 2012.

[65] S. Kang, Y. Mo, S. P. Ong, and G. Ceder. A Facile Mechanism for Recharging Li2O2 in Li-O2 Batteries. *Chemistry of Materials*, 25, 2013.

[66] K. M Abraham. A polymer electrolyte-based rechargeable lithium/oxygen battery. *Journal of The Electrochemical Society*, 143, 1996.

[67] R. Wortmann. Li7O2Br3 - a further structure variant of the new alkali metal chalcogenide halide perovskites. *Zeitschrift fur Naturforschung. B, A journal of chemical sciences*, 44, 1989.

[68] A. M. Glazer. The classification of tilted octahedra in perovskites. *Acta Crystallographica Section B Structural Crystallography and Crystal Chemistry*, 28:3384, 1972.

[69] S. Ping Ong, L. Wang, B. Kang, and G. Ceder. Li?Fe?P?O2 Phase Diagram from First Principles Calculations. *Chemistry of Materials*, 20, 2008.

[70] G. Makov and M. Payne. Periodic boundary conditions in ab initio calculations. *Physical Review B*, 51, 1995.

[71] J. Bhattacharya and A. Van der Ven. Phase stability and nondilute Li diffusion in spinel Li1+xTi2O4. *Physical Review B*, 81, 2010.

[72] J. Bhattacharya and A. Van der Ven. First-principles study of competing mechanisms of nondilute Li diffusion in spinel LixTiS2. *Physical Review B*, 83, 2011.

[73] C. Delmas, C. Fouassier, and P. Hagenmuller. Structural classification and properties of the layered oxides. *Physica B+C*, 99, 1980.

[74] M. S. Whittingham. Lithium Batteries and Cathode Materials. *Chemical Reviews*, 104, 2004.

[75] M. S. Whittingham. Chemistry of intercalation compounds: Metal guests in chalcogenide hosts. *Progress in Solid State Chemistry*, 12, 1978.

[76] S. A. Safran. Stage Ordering in Intercalation Compounds. *Solid State Physics*, 40, 1987.

[77] J. R. Dahn and R. R. Haering. Anomalous bragg peak widths in LixTiS2. *Solid State Communications*, 40, 1981.

[78] A. Van der Ven, M. Aydinol, and G. Ceder. First?Principles Evidence for Stage Ordering in Li x CoO2. *Journal of The Electrochemical Society*, 145, 1998.

[79] Z. Chen, Z. Lu, and J.R. Dahn. Staging Phase Transitions in LixCoO2. *Journal of The Electrochemical Society*, 149, 2002.

[80] J. Bhattacharya and A. Van der Ven. First-principles study of competing mechanisms of nondilute Li diffusion in spinel Li_xTiS_2. *Physical Review B*, 83, 2011.

[81] S. Sinha and D. Murphy. Lithium intercalation in cubic TiS2. *Solid State Ionics*, 20, 1986.

[82] A. Van der Ven, G. Ceder, M. Asta, and P. Tepesch. First-principles theory of ionic diffusion with nondilute carriers. *Physical Review B*, 64, 2001.

[83] M. S. Whittinham. The Role of Ternary Phases in Cathode Reactions. *Journal of The Electrochemical Society*, 123, 1976.

[84] Wolverton C. and A. Zunger. First-Principles Prediction of Vacancy Order-Disorder and Intercalation Battery Voltages in LixCoO2. *Physical Review Letters*, 81, 1998.

[85] M. Aydinol, A. Kohan, G. Ceder, K. Cho, and J. Joannopoulos. Ab initio study of lithium intercalation in metal oxides and metal dichalcogenides. *Physical Review B*, 56, 1997.

[86] A. Van der Ven, J. Bhattacharya, and A. A. Belak. Understanding Li diffusion in Li-intercalation compounds. *Accounts of chemical research*, 46, 2013.

[87] J. Bhattacharya and A. Van der Ven. Phase stability and nondilute Li diffusion in spinel $Li_{1+x}Ti_2O_4$. *Physical Review B*, 81, 2010.

[88] K. Kang and G. Ceder. Factors that affect Li mobility in layered lithium transition metal oxides. *Physical Review B*, 74, 2006.

[89] J. Molenda, C. Delmas, and P. Hagenmuller. Electronic and electrochemical properties of NaxCoO2y cathode. *Solid State Ionics*, 9-10, 1983.

[90] C. Delmas, J.-J. Braconnier, C. Fouassier, and P. Hagenmuller. Electrochemical intercalation of sodium in NaxCoO2 bronzes. *Solid State Ionics*, 3-4, 1981.

[91] A. S. Nagelberg and W Worrell. A thermodynamic study of sodium-intercalated TaS2 and TiS2. *Journal of Solid State Chemistry*, 29, 1979.

[92] J. M. Tarascon and G. W. Hull. Sodium intercalation into the layer oxides NaxMo2O4. *Solid State Ionics*, 22, 1986.

[93] P. Barpanda, G. Oyama, S.-I. Nishimura, S.-C. Chung, and A Yamada. A 3.8-V earth-abundant sodium battery electrode. *Nature Communications*, 5, 2014.

[94] S.-W. Kim, D.-H. Seo, X. Ma, G. Ceder, and K Kang. Electrode Materials for Rechargeable Sodium-Ion Batteries: Potential Alternatives to Current Lithium-Ion Batteries. *Advanced Energy Materials*, 7, 2012.

[95] J. Xu, D. H. Lee, R. J. Clment, X. Yu, M. Leskes, A. J. Pell, G. Pintacuda, X.-Q. Yang, C. P. Grey, and Y. S. Meng. Identifying the Critical Role of Li Substitution in P2-Na_x [Li_y Ni_z Mn_{1-y-z}]O_2 (0 <x,y,z <1) Intercalation Cathode Materials for High-Energy Na-Ion Batteries. *Chemistry of Materials*, 26, 2014.